

Article

# IMM Filtering Algorithms for a Highly Maneuvering Fighter Aircraft: An Overview

M. N. Radhika<sup>1</sup>, Mahendra Mallick<sup>2,\*</sup>  and Xiaoqing Tian<sup>3</sup> 

<sup>1</sup> Department of Electronics and Communications Engineering, PES College of Engineering, Mandya 571401, India; radhikamn9@gmail.com

<sup>2</sup> Independent Researcher, Anacortes, WA 98221, USA

<sup>3</sup> School of Electrical and Control Engineering, Xi'an University of Science and Technology, Xi'an 710054, China; tianxiaoqing2017@xust.edu.cn

\* Correspondence: mmallick.us@gmail.com

**Abstract:** The trajectory estimation of a highly maneuvering target is a challenging problem and has practical applications. The interacting multiple model (IMM) filter is a well-established filtering algorithm for the trajectory estimation of maneuvering targets. In this study, we present an overview of IMM filtering algorithms for tracking a highly-maneuverable fighter aircraft using an air moving target indicator (AMTI) radar on another aircraft. This problem is a nonlinear filtering problem due to nonlinearities in the dynamic and measurement models. We first describe single-model nonlinear filtering algorithms: the extended Kalman filter (EKF), unscented Kalman filter (UKF), and cubature Kalman filter (CKF). Then, we summarize the IMM-based EKF (IMM-EKF), IMM-based UKF (IMM-UKF), and IMM-based CKF (CKF). In order to compare the state estimation accuracies of the IMM-based filters, we present a derivation of the posterior Cramér-Rao lower bound (PCRLB). We consider fighter aircraft traveling with accelerations 3g, 4g, 5g, and 6g and present numerical results for state estimation accuracy and computational cost under various operating conditions. Our results show that under normal operating conditions, the three IMM-based filters have nearly the same accuracy. This is due to the accuracy of the measurements of the AMTI radar and the high data rate.

**Keywords:** highly maneuvering fighter aircraft; extended Kalman filter (EKF); unscented Kalman filter (CKF); cubature Kalman filter (CKF); interacting multiple model (IMM) filter; IMM-EKF; IMM-UKF; IMM-CKF; posterior Cramér-Rao lower bound (PCRLB); measures of performance



**Citation:** Radhika, M.N.; Mallick, M.; Tian, X. IMM Filtering Algorithms for a Highly Maneuvering Fighter Aircraft: An Overview. *Algorithms* **2024**, *17*, 399. <https://doi.org/10.3390/a17090399>

Academic Editor: Constantin Paleologu

Received: 12 July 2024

Revised: 2 September 2024

Accepted: 3 September 2024

Published: 6 September 2024



**Copyright:** © 2024 by the authors. Licensee MDPI, Basel, Switzerland. This article is an open access article distributed under the terms and conditions of the Creative Commons Attribution (CC BY) license (<https://creativecommons.org/licenses/by/4.0/>).

## 1. Introduction

The trajectory estimation of a highly maneuvering fighter aircraft is a challenging problem. By utilizing data obtained from an air moving target indicator (AMTI) radar system, we delve into estimating the trajectory of such a highly maneuvering fighter aircraft. The AMTI radar is on another aircraft, and it measures the range, azimuth, and radial velocity of a target. The AMTI measurement model is nonlinear since the AMTI measurements are nonlinear functions of the target state. The fighter aircraft is capable of flying with motions of nearly constant velocity (NCV) and nearly constant turn (NCT). The NCV model is linear, while the NCT model is nonlinear. The filtering problem is nonlinear since the measurement and dynamic models are nonlinear. An accelerating target is called a maneuvering target [1]. Aircraft that have an acceleration of 3g or higher are considered to be highly maneuvering, where  $g$  is gravitational acceleration and is quantified as  $9.8 \text{ m/s}^2$ . Typical commercial aircraft are restricted to velocities that do not exceed the speed of one Mach, where 1 Mach = 343 m/s [2]. For example, a Boeing 747-8i, Airbus A380, Boeing 787, and a Boeing 777 have maximum speeds of 0.86 Mach, 0.85 Mach, 0.85 Mach, and 0.84 Mach, respectively [2]. Commercial aircraft are typically capable of achieving a maximum rotational acceleration equivalent to approximately three

times gravitational acceleration [3–5]. The maneuverability of a target increases with the  $g$ -value. The maximum  $g$ -value of a fighter aircraft is about  $9g$ . In this study, we take into account aircraft capable of withstanding accelerations ranging from three times to six times gravitational acceleration.

A maneuvering target usually has multiple motions during its travel. This poses a challenge for a filtering algorithm to estimate the states of such targets. In real-world problems, the times at which the motion of a maneuvering target changes are not known. Therefore, the trajectory estimation of a target undergoing various motion dynamics during its maneuvers is significantly harder than that of a target with a single motion.

The Kalman filter (KF) [6–11], extended KF (EKF) [7–13], unscented KF (UKF) [10,11,14,15], Gauss–Hermite filter (GHF) [16], central difference filter (CDF) [16], divided difference filter (DDF) [17], cubature Kalman filter (CKF) [18], and particle filter (PF) [19–22] are single-model filters based on the Bayesian framework. When a target moves with a single motion, these filters are applicable to the filtering problem. The KF operates on the premise of linear dynamics and observation models, incorporating both process noise and measurement noise modeled as additive Gaussian distributions. Given these assumptions and a prior Gaussian distribution, the KF is considered optimal when evaluated under the criterion of minimizing the mean square error (MSE) [7,8,20]. In scenarios where the system dynamics and/or observation models exhibit nonlinear characteristics, the original KF equations are not applicable to the filtering problem, and the EKF, UKF, GHF, CDF, DDF, CKF, and PF are used instead. These filters are approximate or sub-optimal in the MMSE sense. The EKF, UKF, GHF, CDF, DDF, and CKF are based on Gaussian approximation [16,23], and the PF is based on Monte Carlo techniques [19–22]. The EKF, UKF, and CKF are widely used in nonlinear filtering. Therefore, we have chosen these three filtering techniques for tracking an aircraft that engages in complex maneuvers. The computational cost to attain an equivalent level of precision to that of these three filters is a few hundred times more for the PF [24]. Therefore, we have excluded the PF from this study. Detailed explanations are given later.

The EKF [9–13] garnered significant attention following its successful application in the Apollo lunar program. The EKF uses the linearization of the time-evolution function and measurement function by using the Taylor series expansion [7,8]. Previous researchers have found that when the dynamic and measurement models are highly nonlinear and the measurement accuracy is low, the EKF could potentially exhibit sub-optimal performance, and there is a risk that the filter might experience divergence [14,15]. Jullier and Uhlmann introduced the UKF, which incorporates unscented transformation (UT) [14,15], to obtain an improved filtering algorithm. The UKF approximates the posterior probability density function (pdf) by utilizing a collection of  $2n + 1$  sigma points, which are deterministically selected, alongside their respective weights, where  $n$  is the dimension of the state vector. By using a third-degree spherical-radial cubature rule, Arasaratnam and Haykin [19] introduced an innovative approach to the formulation of the CKF. The CKF has  $2n$  deterministic cubature points and associated weights, where each weight is  $1/2n$ . The CKF is regarded as a simple, stable, and effective algorithm for a nonlinear filtering problem based on sound theoretical foundations.

The NCV is a nonmaneuvering motion, whereas nearly constant acceleration (NCA), nearly constant jerk (NCJ), and NCT with an unknown angular velocity are maneuvering motions [1,8]. The models for NCA and NCJ present linear characteristics when considering the Cartesian co-ordinates of the target state. Conversely, the NCT model introduces nonlinearity into the target state representation if the angular velocity remains unspecified. In general, a target can move with a sequence of nonmaneuvering and maneuvering motions. In scenarios where a target exhibits a variety of movement patterns, the times of change in motion are usually unknown. For such a target, the continuous-valued kinematic state (known as the base state) and the discrete-valued mode (known as the modal state) or dynamic model change with time [8]. This class of problems is known as the hybrid state estimation or the jump Markov state estimation problem [8,20,25]. A dynamic model describes the time evolution of the base state by using a stochastic difference equation. The

modal state can assume a finite number of possible values and can switch from one mode to another over time. A homogeneous Markov chain with a known transition probability matrix (TPM) describes changes in the modal state [8,20,25]. In a hybrid state estimation algorithm, a bank of mode-matched filters is run in parallel, and an algorithm to manage the co-operation among the filters is used. The generalized pseudo-Bayesian (GPB) [8,25] algorithm and the interacting multiple model (IMM) algorithm were proposed by Blom et al. [26,27] and are examples of hybrid state estimation algorithms. The  $k$ th-order GPB algorithm is denoted by GPB $k$  and requires  $n_m^k$  filters, where  $n_m$  is the number of models, and  $k$  is the number of sampling periods over which mode switching is considered. In contrast, the IMM algorithm always uses  $n_m$  filters, and the performance of the IMM algorithm is comparable to that of the GPB2 algorithm (which uses  $n_m^2$  filters) at a much reduced computational cost. The computational complexity of the IMM algorithm is nearly linear in the number of models with a small quadratic term. An attractive feature of the IMM algorithm is its modularity [25], which allows it to be used with any filter, such as the KF, EKF, UKF, CKF, etc. The IMM approach has been effectively utilized in a broad spectrum of applications [28–37]. Comprehensive insights into the algorithm, along with an extensive review, can be found in [8] and [25], respectively.

If a single-model filter (e.g., KF, EKF, UKF, or CKF) is used for a maneuvering target, then a high level of process noise will be chosen with a nonmaneuvering motion (e.g., NCV) used to handle maneuvering motion. For this choice, the filter will perform well in the maneuvering segments of the trajectory, but its performance will be poor in the nonmaneuvering segments. If a low level of process noise is chosen, then the filter will perform well in the nonmaneuvering segments, but it will have large errors in the maneuvering segments. On the other hand, the IMM filter will perform well in the nonmaneuvering and maneuvering segments since it probabilistically chooses the motion models. The IMM algorithm also finds application in multi-target tracking (MTT), which refers to the problem of jointly estimating the number of targets and their states from noisy sensor measurements in the presence of a false alarm and a sensor probability of detection that is less than unity [38–42]. MTT problems occur in both civilian and military domains and arise in air traffic control (ATC), ground surveillance, maritime surveillance, airborne surveillance, space-object tracking, autonomous vehicles, ballistic missile defense, [8,25,38,40,43–45], robotics, remote sensing, computer vision, biomedical research, etc. In general, a tracking scenario includes nonmaneuvering and maneuvering targets. Well-known MTT algorithms are the joint probabilistic data association filter (JPDAF) [38,43], multiple hypothesis tracker (MHT) [38–41,44], and random finite set (RFS)-based algorithms [41,42,45]. The IMM algorithm has been successfully used in the multiscan JPDAF [43], MHT [46] and RFS-based algorithms [47]. If a single-model filtering algorithm is used in a multi-target tracker for maneuvering targets, then the measurements will not be associated with predicted tracks due to model mismatch, and tracks will be terminated after a few scans. This will create many tracks corresponding to a true target trajectory. This phenomenon is known as track fragmentation. The fraction of correct measurements in a track, known as the track purity, will also be affected. In general, an IMM-based multi-target tracker will have a significant advantage over a single-model filter-based tracker. Since computer hardware and software systems have improved significantly over the last few decades, IMM-based multi-target trackers can solve complex tracking problems involving nonmaneuvering and maneuvering targets.

The organization of the study is as follows. Section 2 presents the single-model nonlinear filtering algorithms. The hybrid state estimation needed for a maneuvering target is explained in Section 3. Sections 4 and 5 describe the dynamic and measurement models used in the current problem. The EKF, UKF, and CKF are explained in Section 6. The IMM algorithm based on the CKF and PCRLB are discussed in Sections 7 and 8, respectively. The numerical simulation and results for the 3g, 4g, 5g, and 6g cases for various operating conditions are presented in Section 10. Finally, Section 11 provides a summary of the work in the study and discusses the future directions of this research.

## 2. Single-Model Nonlinear Filtering Algorithms

Many real-world filtering problems are nonlinear due to the nonlinearities in the dynamic and measurement models. Measurements of the sonar, radar, electro-optical, GMTI radar, AMTI radar, synthetic aperture radar, over-the-horizon radar, passive radar, video,IRST sensor, unattended ground sensor, and 2D air traffic control radar are nonlinear functions of the target state [20,40,48]. The NCT model with an unknown turn rate and dynamic models involving atmospheric drag, as well as the gravitational forces of the earth, moon, sun, and other planets, are nonlinear in the target state [49]. The sensor measurement models are always discrete, as the data are gathered at specific intervals. A dynamic model can be continuous or discrete in time. The dynamic models for an earth-orbiting satellite [49], ballistic missile, and ballistic projectile are continuous in time and are described by stochastic differential equations [50]. These filtering problems are known as continuous-discrete filtering problems. Most filtering problems in target tracking are discrete in nature, where the dynamic and measurement models are both discrete. In this study, we consider discrete filtering problems. Next, we discuss the general single-model filtering.

### 2.1. Single-Model Filtering

Let  $\mathbf{x}_k$  and  $\mathbf{z}_k$  denote the  $n$ -dimensional and  $m$ -dimensional target state and sensor measurement at time  $t_k$ . The discrete-time dynamic and measurement models for a nonlinear filtering problem are described by [8,20]

$$\mathbf{x}_k = \mathbf{f}_{k-1}(\mathbf{x}_{k-1}) + \mathbf{w}_{k-1}, \quad (1)$$

$$\mathbf{z}_k = \mathbf{h}_k(\mathbf{x}_k) + \mathbf{n}_k, \quad (2)$$

where  $\mathbf{f}_{k-1}$  and  $\mathbf{h}_k$  are known functions for time evolution and measurement, respectively. We assume that the process noise  $\mathbf{w}_{k-1}$  is zero-mean white Gaussian for the time interval  $(t_{k-1}, t_k]$  with a covariance of  $\mathbf{Q}_{k-1}$  and that the measurement noise  $\mathbf{n}_k$  is zero-mean white Gaussian with a covariance of  $\mathbf{R}_k$  at time  $t_k$  [8,20]. Our goal is to process the noisy measurements sequentially and estimate the target state. Next, we present the formal recursive Bayesian optimal estimation approach [20,50]. Let  $\mathbf{Z}_k$  represent the complete collection of observations accumulated up to the time  $t_k$ ,

$$\mathbf{Z}_k := \{\mathbf{z}_1, \mathbf{z}_2, \dots, \mathbf{z}_k\}. \quad (3)$$

The conditional mean represents the optimal estimate in the MMSE sense and is given by [7,8,20,50]

$$\hat{\mathbf{x}}_{k|k} = E\{\mathbf{x}_k | \mathbf{Z}_k\} = \int \mathbf{x}_k p(\mathbf{x}_k | \mathbf{Z}_k) d\mathbf{x}_k, \quad (4)$$

where  $p(\mathbf{x}_k | \mathbf{Z}_k)$  represents the conditional probability density function (pdf). Suppose we know the pdf  $p(\mathbf{x}_{k-1} | \mathbf{Z}_{k-1})$  at time  $t_{k-1}$ . Our objective is to determine the posterior pdf  $p(\mathbf{x}_k | \mathbf{Z}_k)$  after processing the measurement  $\mathbf{z}_k$ . At time  $t_k$ , the prediction density or prior density is given by the Chapman-Kolmogorov equation [20,50].

$$p(\mathbf{x}_k | \mathbf{Z}_{k-1}) = \int p(\mathbf{x}_k | \mathbf{x}_{k-1}) p(\mathbf{x}_{k-1} | \mathbf{Z}_{k-1}) d\mathbf{x}_{k-1}, \quad (5)$$

where  $p(\mathbf{x}_k | \mathbf{x}_{k-1})$  is the transition density. By using Bayes' rule, we obtain the posterior density:

$$p(\mathbf{x}_k | \mathbf{Z}_k) = \frac{p(\mathbf{z}_k | \mathbf{x}_k) p(\mathbf{x}_k | \mathbf{Z}_{k-1})}{p(\mathbf{z}_k | \mathbf{Z}_{k-1})}, \quad (6)$$

where the normalization constant is given by

$$p(\mathbf{z}_k | \mathbf{Z}_{k-1}) = \int p(\mathbf{z}_k | \mathbf{x}_k) p(\mathbf{x}_k | \mathbf{Z}_{k-1}) d\mathbf{x}_k. \quad (7)$$

The quantity  $p(\mathbf{z}_k|\mathbf{x}_k)$  is known as the likelihood of the state  $\mathbf{x}_k$  given the measurement  $\mathbf{z}_k$  [8]. From the dynamic model (1) with additive zero-mean white Gaussian noise,  $\mathbf{w}_{k-1}$ , with a covariance of  $\mathbf{Q}_{k-1}$ , we obtain the transition density as

$$p(\mathbf{x}_k|\mathbf{x}_{k-1}) = \mathcal{N}(\mathbf{x}_k; \mathbf{f}_{k-1}(\mathbf{x}_{k-1}), \mathbf{Q}_{k-1}). \tag{8}$$

Similarly, from the measurement model (2) with additive zero-mean Gaussian noise,  $\mathbf{n}_k$ , with a covariance of  $\mathbf{R}_k$ , the likelihood can be expressed as

$$p(\mathbf{z}_k|\mathbf{x}_k) = \mathcal{N}(\mathbf{z}_k; \mathbf{h}_k(\mathbf{x}_k), \mathbf{R}_k). \tag{9}$$

Given the prior distribution  $p_0(\mathbf{x}_0)$  of the target state, in principle, we can recursively determine the posterior density  $p(\mathbf{x}_k|\mathbf{Z}_k)$  using (5)–(9). However, obtaining closed-form solutions is intractable in most cases due to multi-dimensional integrals in (5) and (7), and in most real-world problems, approximate or sub-optimal solutions are obtained. The EKF, UKF, CKF, GHF, CDF, DDF, and PF represent examples of approximate nonlinear filters. If we assume that all the densities are Gaussian, then the Bayesian recursion Equations (5)–(7) can be evaluated approximately, and the resulting class of filters is called Gaussian filters [16,20,23]. The Gaussian approximation to  $p(\mathbf{x}_k|\mathbf{Z}_k)$  is specified by the mean  $\hat{\mathbf{x}}_{k|k}$  and covariance  $\mathbf{P}_{k|k}$  and is given by

$$p(\mathbf{x}_k|\mathbf{Z}_k) \approx \mathcal{N}(\mathbf{x}_k; \hat{\mathbf{x}}_{k|k}, \mathbf{P}_{k|k}), \tag{10}$$

where

$$\hat{\mathbf{x}}_{k|k} = \hat{\mathbf{x}}_{k|k-1} + \mathbf{K}_k \mathbf{v}_k, \tag{11}$$

$$\mathbf{P}_{k|k} = \mathbf{P}_{k|k-1} - \mathbf{K}_k \mathbf{P}_{\mathbf{z}\mathbf{z},k} \mathbf{K}'_k, \tag{12}$$

$$\mathbf{v}_k := \mathbf{z}_k - \hat{\mathbf{z}}_{k|k-1}, \tag{13}$$

$$\mathbf{K}_k = \mathbf{P}_{\mathbf{x}\mathbf{z},k} \mathbf{P}_{\mathbf{z}\mathbf{z},k}^{-1}, \tag{14}$$

and  $\hat{\mathbf{x}}_{k|k-1}$  and  $\mathbf{P}_{k|k-1}$  denote the predicted mean and predicted covariance, respectively. In (11)–(14),  $\hat{\mathbf{z}}_{k|k-1}$ ,  $\mathbf{v}_k$ ,  $\mathbf{P}_{\mathbf{z}\mathbf{z},k}$ , and  $\mathbf{K}_k$  represent the predicted measurement, innovation, innovation covariance, and Kalman gain, respectively [8,16,20]. The matrix  $\mathbf{P}_{\mathbf{x}\mathbf{z},k}$  is the cross-covariance between the prediction error and innovation. The various terms appearing in (11)–(14) are given by

$$\hat{\mathbf{x}}_{k|k-1} = E\{\mathbf{x}_k|\mathbf{Z}_{k-1}\} = E\{\mathbf{f}_{k-1}(\mathbf{x}_{k-1})|\mathbf{Z}_{k-1}\}, \tag{15}$$

$$\mathbf{P}_{k|k-1} = \mathbf{Q}_{k-1} + E\{(\mathbf{f}_{k-1}(\mathbf{x}) - \hat{\mathbf{x}}_{k|k-1})(\mathbf{f}_{k-1}(\mathbf{x}) - \hat{\mathbf{x}}_{k|k-1})'|\mathbf{Z}_{k-1}\}, \tag{16}$$

$$\hat{\mathbf{z}}_{k|k-1} = E\{\mathbf{z}_k|\mathbf{Z}_{k-1}\} = E\{\mathbf{h}_k(\mathbf{x}_k)|\mathbf{Z}_{k-1}\}, \tag{17}$$

$$\mathbf{P}_{\mathbf{x}\mathbf{z},k} = E\{(\mathbf{x}_k - \hat{\mathbf{x}}_{k|k-1})(\mathbf{h}_k(\mathbf{x}_k) - \hat{\mathbf{z}}_{k|k-1})'|\mathbf{Z}_{k-1}\}, \tag{18}$$

$$\mathbf{P}_{\mathbf{z}\mathbf{z},k} = \mathbf{R}_k + E\{(\mathbf{x}_k - \hat{\mathbf{x}}_{k|k-1})(\mathbf{h}_k(\mathbf{x}_k) - \hat{\mathbf{z}}_{k|k-1})'|\mathbf{Z}_{k-1}\}. \tag{19}$$

### 2.2. Gaussian Filters

The EKF, UKF, CKF, GHF, CDF, and DDF belong to the class of Gaussian filters. These filters evaluate the expected values appearing in (15)–(19) differently using Gaussian approximation. In general, a filter has two steps: prediction (or time update) and measurement update. The prediction and measurement update steps are governed by (15)–(17) and (11)–(14), as well as (18) and (19), respectively. The EKF linearizes the nonlinear functions  $\mathbf{f}_{k-1}$  and  $\mathbf{h}_k$  for estimates  $\hat{\mathbf{x}}_{k-1|k-1}$  and  $\hat{\mathbf{x}}_{k|k-1}$  using the Taylor series expansion, and then it computes the expected values in (15)–(19) [8,20,50]. It was observed in some cases that the EKF does not work well and diverges when the degree of nonlinearity is high, the measurement accuracy is low, and the measurement time interval is high. The Cartesian



EKF diverges for the bearing-only filtering problem, which satisfies these conditions [20]. It is easier to approximate a pdf than to approximate a nonlinear function. UT [14] and cubature transformation (CT) [18] use this concept to represent the mean and covariance of a Gaussian-distributed random variable using sigma points and cubature points, respectively. When a nonlinear function such as  $\mathbf{f}_{k-1}$  or  $\mathbf{h}_k$  transforms a Gaussian random variable, the sigma points and cubature points are used to obtain the more accurate mean and covariance of the transformed random variable than those obtained by the Taylor series expansion. The UKF based on the UT and the CKF based on the CT yield more precise outcomes compared to the EKF in such cases. The PF or sequential Monte Carlo is an approximate filter that implements the recursive Bayesian algorithm in (5)–(7) using Monte Carlo simulations [19,20]. There are many versions of the PF [19,20]. In a PF, the posterior pdf is represented by a set of random samples or particles and associated weights  $\{\mathbf{x}_k^i, w_k^i\}_{i=1}^N$ , where  $N$  is the number of particles. As the number of particles increases, the discrete approximation of the pdf approaches the true pdf, and the particle-based estimates approach the optimal estimates. The number of particles depends on the nonlinear filtering problem. The sequential importance sampling algorithm is a commonly used method in a PF [19,20].

### 3. Hybrid State Estimation

Suppose a target can have  $n_m$  modes or dynamic models. Let  $m_k$  be the mode during the time interval  $(t_{k-1}, t_k]$ . The dynamic and measurement models for a hybrid system are given by [8,20,25]

$$\mathbf{x}_k = \mathbf{f}_{k-1}(\mathbf{x}_{k-1}, m_k) + \mathbf{w}_{k-1}(m_k), \tag{20}$$

$$\mathbf{z}_k = \mathbf{h}_k(\mathbf{x}_k, m_k) + \mathbf{n}_k(m_k). \tag{21}$$

The time variation of the modal state is described by a homogeneous Markov chain with known  $n_m \times n_m$  TPM  $\mathbf{\Pi}$  [8,20,25]:

$$\pi_{ij} := P(m_k = j | m_{k-1} = i), \quad i, j = 1, 2, \dots, n_m, \tag{22}$$

where  $\pi_{ij}$  is the  $(i, j)$ th matrix element of  $\mathbf{\Pi}$ . The transition probabilities satisfy

$$\pi_{ij} > 0 \text{ and } \sum_{j=1}^{n_m} \pi_{ij} = 1, \text{ for } i, j = 1, 2, \dots, n_m. \tag{23}$$

Let  $\{\mu_i\}$  denote the initial model probabilities defined by  $\mu_i := P(m_1 = i)$ ,  $i = 1, 2, \dots, n_m$  and satisfying

$$\mu_i > 0, \text{ for } i = 1, 2, \dots, n_m \text{ and } \sum_{i=1}^{n_m} \mu_i = 1. \tag{24}$$

The state of the hybrid system at time  $t_k$  is the augmented state  $\mathbf{y}_k = [\mathbf{x}_k' \quad m_k]'$ . For the formal recursive equations, interested readers may refer to Section 1.4 of [20]. Detailed steps of the hybrid state estimation algorithm using the IMM-CKF algorithm are described in Section 5.

### 4. Dynamic Models

For all dynamic models, we use the discretized continuous-time model [8]. Let  $(x, y)$  and  $(\dot{x}, \dot{y})$  denote the Cartesian position and velocity of the aircraft state, respectively. At time  $t_k$ , the state of the aircraft in both the NCV and NCT models is defined as follows [20,51]:

$$\mathbf{x}_k := [x_k \quad y_k \quad \dot{x}_k \quad \dot{y}_k]'. \tag{25}$$

The counterclockwise and clockwise NCT motions are denoted by NCT+ and NCT-, respectively. Within the scope of this study, the NCV, NCT+, and NCT- are each assigned to model numbers 1, 2, and 3, respectively. Furthermore, the model indices are indicated in

superscript form within the state transition matrix, time evolution function, the vector of the process noise, and the matrix of process noise covariance [20,51].

#### 4.1. Nearly Constant Velocity (NCV) Model

The dynamics of the NCV movement are captured through a linear model, which is described by [5,8,20]:

$$\mathbf{x}_k = \mathbf{F}_{k-1}^{(1)} \mathbf{x}_{k-1} + \mathbf{w}_{k-1}^{(1)}, \tag{26}$$

where  $\mathbf{F}_{k-1}^{(1)}$  is the state transition matrix and  $\mathbf{w}_{k-1}^{(1)}$  represents the process noise during the interval from  $t_{k-1}$  to  $t_k$ . Assuming  $\mathbf{w}_{k-1}^{(1)}$  to be zero-mean Gaussian white noise with the covariance matrix  $\mathbf{Q}_{k-1}^{(1)}$ , the corresponding definitions for  $\mathbf{F}_{k-1}^{(1)}$  and  $\mathbf{w}_{k-1}^{(1)}$  are as follows [5,8,20]:

$$\mathbf{F}_{k-1}^{(1)} = \begin{bmatrix} 1 & 0 & T & 0 \\ 0 & 1 & 0 & T \\ 0 & 0 & 1 & 0 \\ 0 & 0 & 0 & 1 \end{bmatrix}, \tag{27}$$

$$E\{\mathbf{w}_{k-1}^{(1)}\} = \mathbf{0}_{4 \times 1} \tag{28}$$

$$E\{\mathbf{w}_{i-1}^{(1)} \mathbf{w}_{k-1}^{(1)T}\} = \delta_{jk} \mathbf{Q}_{i-1}^{(1)} \tag{29}$$

$$\mathbf{Q}_{k-1}^{(1)} = q_1 \begin{bmatrix} T^3/3 & 0 & T^2/2 & 0 \\ 0 & T^3/3 & 0 & T^2/2 \\ T^2/2 & 0 & T & 0 \\ 0 & T^2/2 & 0 & T \end{bmatrix}, \tag{30}$$

where  $\delta$  is the Kronecker delta,  $T$  is the constant measurement time interval, and  $q_1$  denotes the power spectral density (PSD) of the acceleration noise process in continuous time for model 1, which is applicable to both the X and Y components [8,20,51].

#### 4.2. Nearly Constant Turn (NCT) Model

The dynamics of the NCT movement are captured through a nonlinear model, which is described by [5,8,20]

$$\mathbf{x}_k = \mathbf{f}^{(j)}(\mathbf{x}_{k-1}) + \mathbf{w}_{k-1}^{(j)}, \tag{31}$$

where

$$\mathbf{f}^{(j)}(\mathbf{x}_{k-1}) := \mathbf{A}^{(j)}(\mathbf{x}_{k-1}) \mathbf{x}_{k-1}, \quad j = 2, 3, \tag{32}$$

$$\mathbf{A}^{(j)}(\mathbf{x}_{k-1}) = \begin{bmatrix} 1 & 0 & \frac{\sin(\omega_{k-1}^{(j)} T)}{\omega_{k-1}^{(j)}} & -\frac{1 - \cos(\omega_{k-1}^{(j)} T)}{\omega_{k-1}^{(j)}} \\ 0 & 1 & \frac{1 - \cos(\omega_{k-1}^{(j)} T)}{\omega_{k-1}^{(j)}} & \frac{\sin(\omega_{k-1}^{(j)} T)}{\omega_{k-1}^{(j)}} \\ 0 & 0 & \cos(\omega_{k-1}^{(j)} T) & -\sin(\omega_{k-1}^{(j)} T) \\ 0 & 0 & \sin(\omega_{k-1}^{(j)} T) & \cos(\omega_{k-1}^{(j)} T) \end{bmatrix}, \quad j = 2, 3. \tag{33}$$

In (33), the angular velocity  $\omega_{k-1}^{(j)}$  at time  $t_{k-1}$  for model  $j$  is given by

$$\omega_{k-1}^{(j)} = \kappa^{(j)} \frac{a_m}{\sqrt{\dot{x}_{k-1}^2 + \dot{y}_{k-1}^2}}, \quad j = 2, 3, \tag{34}$$

where  $a_m > 0$  signifies a standard maneuvering acceleration, while  $\kappa^{(2)}$  and  $\kappa^{(3)}$  are indicators with values of 1 and  $-1$  for the NCT+ and NCT- maneuvers, respectively. The covariance matrices of  $\omega_{k-1}^{(2)}$  and  $\omega_{k-1}^{(3)}$  are defined as follows [20,51]:

$$\mathbf{Q}_{k-1}^{(j)} = q_j \begin{bmatrix} T^3/3 & 0 & T^2/2 & 0 \\ 0 & T^3/3 & 0 & T^2/2 \\ T^2/2 & 0 & T & 0 \\ 0 & T^2/2 & 0 & T \end{bmatrix}, \quad j = 2, 3, \quad (35)$$

where  $q_2$  and  $q_3$  denote the PSDs of the noise processes in models 2 and 3, respectively [3], with  $q_2 = q_3$ .

### 5. Measurement Model

The AMTI radar measures the range, bearing (or azimuth), and radial velocity of the target [52]. Figure 1 [51] depicts the true range,  $r_k$ , azimuth,  $\beta_k$ , and radial velocity,  $v_{r,k}$  of the target at time  $t_k$ . Assume that the radar moves with CV. At time  $t_k$ , the state vector of the AMTI radar is given by

$$\mathbf{x}_k^s = [x_k^s \quad y_k^s \quad \dot{x}_k^s \quad \dot{y}_k^s]'. \quad (36)$$

The position and velocity vectors of the target denoted by  $\mathbf{p}_k$  and  $\mathbf{v}_k$ , respectively, at time  $t_k$  are specified by

$$\mathbf{p}_k = [x_k \quad y_k]', \quad (37)$$

$$\mathbf{v}_k = [\dot{x}_k \quad \dot{y}_k]'. \quad (38)$$

Let  $\mathbf{p}_k^s$  denote the position vector of the AMTI radar at time  $t_k$ :

$$\mathbf{p}_k^s = [x_k^s \quad y_k^s]'. \quad (39)$$

The range vector of the target from the AMTI radar at time  $t_k$  is

$$\mathbf{r}_k = \mathbf{p}_k - \mathbf{p}_k^s = [x_k - x_k^s \quad y_k - y_k^s]'. \quad (40)$$

Then, the range of the target from the AMTI radar at time  $t_k$  is given by

$$r_k = \|\mathbf{p}_k - \mathbf{p}_k^s\| = \sqrt{(x_k - x_k^s)^2 + (y_k - y_k^s)^2}. \quad (41)$$

Let  $\mathbf{u}_k$  denote the unit vector along the radar line-of-sight (RLOS). Then,

$$\mathbf{u}_k := \mathbf{r}_k / r_k = \frac{\mathbf{p}_k - \mathbf{p}_k^s}{\|\mathbf{p}_k - \mathbf{p}_k^s\|}. \quad (42)$$

The radial velocity of the target  $v_{r,k}$  at time  $t_k$  is given by [24,52]

$$v_{r,k} = \frac{1}{r_k} [(x_k - x_k^s)\dot{x}_k + (y_k - y_k^s)\dot{y}_k]. \quad (43)$$

Hence, the radial velocity represents the component of the target's velocity that is projected onto the RLOS (Figure 1).

At time  $t_k$ , given the target speed  $v_k$  and the angle between the target velocity and the RLOS  $\alpha_k$ , the radial velocity of the target  $v_{r,k}$  can be calculated as

$$v_{r,k} = v_k \cos \alpha_k. \quad (44)$$



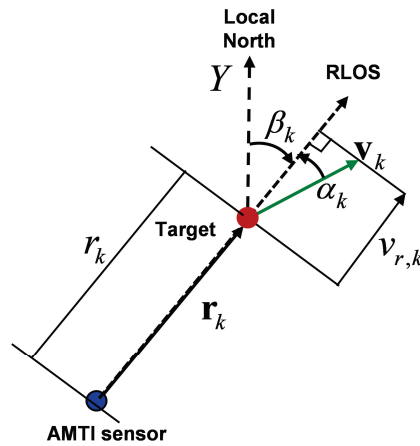


Figure 1. True range, azimuth, and radial velocity [51].

Figure 1 and Equation (44) demonstrate that the radial velocity exhibits its peak values of  $v_k$  and  $-v_k$  when the target moves in the same or opposite direction as the RLOS. It vanishes to zero when the target's velocity is perpendicular to the RLOS. The true trajectories of the AMTI radar and aircraft moving at 3g, 4g, 5g, and 6g are shown in Figure 2, where the red and blue lines indicate the trajectories of the aircraft and AMTI radar, respectively. An open circle and a diamond indicate the start and end points of a trajectory, respectively. Each aircraft trajectory encompasses a succession of motion phases, including segments of NCV, NCT+, another NCV, NCT-, and concluding with another NCV. In Figure 3, different segments of the trajectory of an aircraft moving at 3g are presented, and the durations of various segments with start and end times are also given in Table 1.

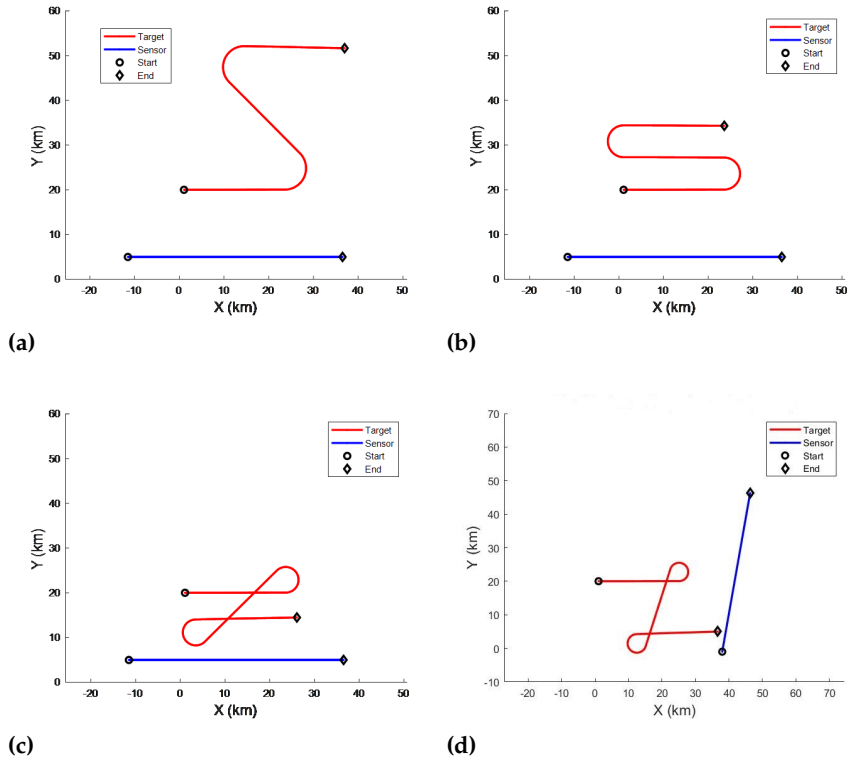
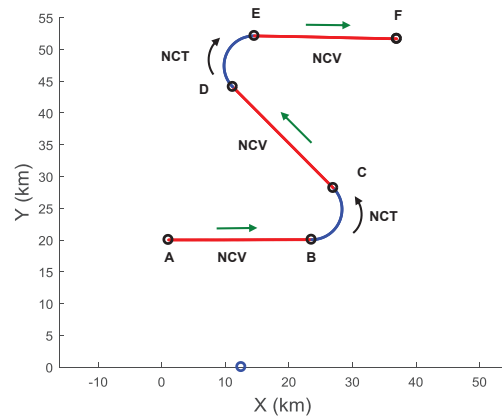


Figure 2. Trajectories of an aircraft moving at (a) 3g, (b) 4g, (c) 5g, and (d) 6g and AMTI sensor trajectories.



**Figure 3.** Different segments of the trajectory of an aircraft moving at 3g.

**Table 1.** Segment lengths and times for the 3g case.

Segment	Length (s)	Initial and Final Times (s)
First NCV, AB	60	[0, 60]
NCT+, BC	30	[60, 90]
Second NCV, CD	60	[90, 150]
NCT-, DE	30	[150, 180]
Third NCV, EF	60	[180, 240]

At time  $t_k$ , the radar measurement vector  $\mathbf{z}_k$  is defined as

$$\mathbf{z}_k = [z_{k,r} \quad z_{k,\beta} \quad v_{k,v_r}]'. \tag{45}$$

The measurement model for the AMTI radar is defined by [52]

$$\mathbf{z}_k = \mathbf{h}(\mathbf{x}_k) + \mathbf{n}_k, \tag{46}$$

where  $\mathbf{h}$  is the nonlinear measurement function

$$\mathbf{h}(\mathbf{x}_k) = \begin{bmatrix} r_k \\ \beta_k \\ v_{r,k} \end{bmatrix} = \begin{bmatrix} \sqrt{(x_k - x_k^s)^2 + (y_k - y_k^s)^2} \\ \tan^{-1}(x_k - x_k^s, y_k - y_k^s) \\ \frac{1}{r_k} [(x_k - x_k^s)\dot{x}_k + (y_k - y_k^s)\dot{y}_k] \end{bmatrix}, \quad \text{with } r_k > 0, \beta_k \in [0, 2\pi). \tag{47}$$

In (46),  $\mathbf{n}_k$  is a zero-mean white Gaussian measurement noise with the covariance matrix  $\mathbf{R}$ . The corresponding definitions of  $\mathbf{n}_k$  are given as follows:

$$\mathbf{n}_k = [n_{k,r} \quad n_{k,\beta} \quad n_{k,v_r}]', \tag{48}$$

$$E\{\mathbf{n}_k\} = \mathbf{0}_{3 \times 1}, \tag{49}$$

$$E\{\mathbf{n}_j \mathbf{n}_k\} = \delta_{jk} \mathbf{R}, \tag{50}$$

$$\mathbf{n}_k \sim \mathcal{N}(\mathbf{n}_k; \mathbf{0}_{3 \times 1}, \mathbf{R}), \tag{51}$$

$$\mathbf{R} = \text{diag}(\sigma_r^2, \sigma_\beta^2, \sigma_{v_r}^2), \tag{52}$$

where  $\sigma_r, \sigma_\beta, \sigma_{v_r}$  are the measurement errors' standard deviations (SDs) for range, azimuth, and radial velocity, respectively. The dynamic model of the radar moving with CV is formulated by

$$\mathbf{x}_k^s = \mathbf{F}_{k-1}^{(1)} \mathbf{x}_{k-1}^s, \tag{53}$$

where  $\mathbf{F}_{k-1}^{(1)}$  is given by (27).

## 6. EKF, UKF, and CKF

Suppose we have the estimated state  $\hat{\mathbf{x}}_{k-1|k-1}$  and associated covariance  $\mathbf{P}_{k-1|k-1}$  at time  $t_{k-1}$ . Our goal is to obtain the estimated state  $\hat{\mathbf{x}}_{k|k}$  and associated covariance  $\mathbf{P}_{k|k}$  at time  $t_k$  after processing the measurement  $\mathbf{z}_k$  at time  $t_k$ . Next, we describe the iteration of obtaining  $\hat{\mathbf{x}}_{k|k}$  and  $\mathbf{P}_{k|k}$  from  $\hat{\mathbf{x}}_{k-1|k-1}$  and  $\mathbf{P}_{k-1|k-1}$  using the nonlinear dynamic and measurement models. We assume that the process noise and measurement noise are zero-mean Gaussian. Consider the discrete-time nonlinear dynamic model in (1). For our problem, the dynamic models for NCV and NCT are given in (26) and (31), respectively. The nonlinear measurement model is given by (46)–(52). The iteration includes a prediction step (also called the time-update step) and a measurement update step.

### 6.1. EKF

#### 6.1.1. Prediction

The predicted state estimate and its associated covariance matrix are given, respectively, by [5,7,8,20]

$$\hat{\mathbf{x}}_{k|k-1} = \mathbf{f}_k(\hat{\mathbf{x}}_{k-1|k-1}), \tag{54}$$

$$\mathbf{P}_{k|k-1} = \mathbf{F}_{k-1}\mathbf{P}_{k-1|k-1}\mathbf{F}'_{k-1} + \mathbf{Q}_{k-1}, \tag{55}$$

where the Jacobian of the time evolution function is given by

$$\mathbf{F}_{k-1} = \left. \frac{\partial \mathbf{f}_k(\mathbf{x})}{\partial \mathbf{x}} \right|_{\mathbf{x}=\hat{\mathbf{x}}_{k-1|k-1}}. \tag{56}$$

#### 6.1.2. Measurement Update

The predicted measurement  $\hat{\mathbf{z}}_{k|k-1}$  and innovation covariance  $\mathbf{P}_{\mathbf{zz},k} = \mathbf{S}_k$  are given by [5,7,8,20]

$$\hat{\mathbf{z}}_{k|k-1} = \mathbf{h}(\hat{\mathbf{x}}_{k|k-1}), \tag{57}$$

$$\mathbf{P}_{\mathbf{zz},k} = \mathbf{S}_k = \mathbf{R}_k + \mathbf{H}_k\mathbf{P}_{k|k-1}\mathbf{H}'_k, \tag{58}$$

where the Jacobian of the measurement function is given by

$$\mathbf{H}_k = \left. \frac{\partial \mathbf{h}(\mathbf{x})}{\partial \mathbf{x}} \right|_{\mathbf{x}=\hat{\mathbf{x}}_{k|k-1}}. \tag{59}$$

The expression for the updated state estimate and covariance in (11)–(14) hold, and the expression for the cross-covariance  $\mathbf{P}_{\mathbf{xz},k}$  is given by [5,8]

$$\mathbf{P}_{\mathbf{xz},k} = \mathbf{P}_{k|k-1}\mathbf{H}'_k. \tag{60}$$

### 6.2. Unified Algorithm of UKF and CKF

Unlike the EKF, the UKF and CKF can operate without the need for derivative calculations. In this study, we use the UT [14] in UKF. The scaled UT (SUT) can also be used in the UKF [15]. In order to present the UKF and CKF in a unified way, we define

$$i_0 = \begin{cases} 0 & \text{for UKF,} \\ 1 & \text{for CKF,} \end{cases} \tag{61}$$

$$\gamma = \begin{cases} n + \kappa & \text{for UKF,} \\ n & \text{for CKF,} \end{cases} \tag{62}$$

where  $\kappa$  is a parameter used in the UT and a value of  $3 - n$  is suggested [14]. Following [18], we summarize the prediction and measurement update steps in Sections 6.2.1 and 6.2.2,

respectively. The UKF utilizes  $2n + 1$  sigma points, whereas the CKF employs  $2n$  cubature points in its computation. Let  $m = 2n$ . The weights used in the UKF and CKF are given by

$$\text{UKF: } w_0 = \frac{\kappa}{\gamma}, \quad w_i = \frac{1}{2\gamma}, \quad \text{for } i = 1, 2, \dots, m, \tag{63}$$

$$\text{CKF: } w_i = \frac{1}{2\gamma}, \quad i = 1, 2, \dots, m. \tag{64}$$

### 6.2.1. Prediction

The following steps describe the computation of the predicted state estimate  $\hat{\mathbf{x}}_{k|k-1}$  and predicted covariance  $\mathbf{P}_{k|k-1}$  at time  $t_k$ .

**Step 1:** Perform a Cholesky decomposition on  $\mathbf{P}_{k-1|k-1}$ ,

$$\mathbf{P}_{k-1|k-1} = \mathbf{S}_{k-1|k-1} \mathbf{S}'_{k-1|k-1}. \tag{65}$$

**Step 2:** Compute the sample points

$$\mathbf{X}_{i,k-1|k-1} = \mathbf{S}_{k-1|k-1} \boldsymbol{\zeta}_i + \hat{\mathbf{x}}_{k-1|k-1}, \quad i = i_0, \dots, m, \tag{66}$$

where

$$\boldsymbol{\zeta}_0 = \mathbf{0}_{n \times 1}, \quad \boldsymbol{\zeta}_i = \sqrt{\gamma} [\mathbf{I}_n \quad -\mathbf{I}_n]_i, \quad i = i_0, \dots, m. \tag{67}$$

Therefore,

$$\mathbf{S}_{k-1|k-1} \boldsymbol{\zeta}_i = \sqrt{\gamma} [\mathbf{S}_{k-1|k-1} \quad -\mathbf{S}_{k-1|k-1}]_i, \quad i = i_0, \dots, m, \tag{68}$$

where  $[\mathbf{S}_{k-1|k-1} \quad -\mathbf{S}_{k-1|k-1}]_i$  is the  $i$ th column of the  $n \times m$  matrix  $[\mathbf{S}_{k-1|k-1} \quad -\mathbf{S}_{k-1|k-1}]$ .

**Step 3:** Propagate the sample points from time  $t_{k-1}$  to time  $t_k$ ,

$$\mathbf{X}^*_{i,k|k-1} = \mathbf{f}_k(\mathbf{X}_{i,k-1|k-1}), \quad i = i_0, \dots, m. \tag{69}$$

**Step 4:** Compute the predicted state estimate at time  $t_k$ ,

$$\hat{\mathbf{x}}_{k|k-1} = \sum_{i=i_0}^m w_i \mathbf{X}^*_{i,k|k-1}. \tag{70}$$

**Step 5:** Compute the predicted error covariance at time  $t_k$ ,

$$\mathbf{P}_{k|k-1} = \sum_{i=i_0}^m w_i \mathbf{X}^*_{i,k|k-1} (\mathbf{X}^*_{i,k|k-1})' - \hat{\mathbf{x}}_{k|k-1} \hat{\mathbf{x}}'_{k|k-1} + \mathbf{Q}_{k-1}. \tag{71}$$

### 6.2.2. Measurement Update

**Step 1:** Perform a Cholesky decomposition on  $\mathbf{P}_{k|k-1}$ ,

$$\mathbf{P}_{k|k-1} = \mathbf{S}_{k|k-1} \mathbf{S}'_{k|k-1} \tag{72}$$

**Step 2:** Compute the cubature points,

$$\mathbf{X}_{i,k|k-1} = \mathbf{S}_{k|k-1} \boldsymbol{\zeta}_i + \hat{\mathbf{x}}_{k|k-1}, \quad i = i_0, \dots, m. \tag{73}$$

**Step 3:** Compute the predicted measurement sample points,

$$\mathbf{Z}_{i,k|k-1} = \mathbf{h}(\mathbf{X}_{i,k|k-1}), \quad i = i_0, \dots, m. \tag{74}$$

**Step 4:** Compute the predicted measurement at time  $t_k$ ,

$$\hat{\mathbf{z}}_{k|k-1} = \sum_{i=i_0}^m w_i \mathbf{Z}_{i,k|k-1}. \tag{75}$$

**Step 5:** Compute the innovation covariance,

$$\mathbf{P}_{\mathbf{zz},k} = \sum_{i=i_0}^m w_i \mathbf{Z}_{i,k|k-1} \mathbf{Z}'_{i,k|k-1} - \hat{\mathbf{z}}_{k|k-1} \hat{\mathbf{z}}'_{k|k-1} + \mathbf{R}_k. \tag{76}$$

**Step 6:** Compute the cross-covariance matrix,

$$\mathbf{P}_{\mathbf{xz},k} = \sum_{i=i_0}^m w_i \mathbf{X}_{i,k|k-1} \mathbf{Z}'_{i,k|k-1} - \hat{\mathbf{x}}_{k|k-1} \hat{\mathbf{z}}'_{k|k-1}. \tag{77}$$

**Step 7:** Compute the updated state estimate and associated covariance at time  $t_k$  using (11)–(14).

### 7. IMM Algorithm Based on CKF

In order to estimate the state of a maneuvering target in a nonlinear filtering problem, the IMM-EKF [29–31,53–56], IMM-UKF [32,54,55,57], IMM-CKF [2,3,58], and IMM-cubature quadrature Kalman filter (IMM-CQKF) [4] are commonly used. The IMM filtering algorithm maintains a common structure across its variations, such as the IMM-EKF, IMM-UKF, and IMM-CKF, with only minor distinctions. In order to conserve space, this section focuses on detailing the IMM-CKF filter. The IMM filter is designed to leverage a collection of kinematic models, encompassing all potential aircraft maneuvers across any trajectory segment [8,20,25,27]. By incorporating a parallel execution of three distinct CKFs, the IMM filter adeptly manages the NCV, NCT+, and NCT- motion models.

Suppose at time  $t_{k-1}$ , the state estimates  $\hat{\mathbf{x}}_{k-1|k-1}^i$ , the covariance matrices  $\mathbf{P}_{k-1|k-1}^i$ , and the model probabilities  $\mu_{k-1}^i$  are available, where  $i = 1, 2, \dots, 3$ . We define the TPM as  $\mathbf{\Pi} \in \mathcal{R}^{3 \times 3}$  with elements  $\{\pi_{ij}\}$  and the probability of the  $i$ th model as  $\mu_k^i$ . Next, we summarize the various steps of the IMM filter [8,20,25,27] to compute the model probabilities, state estimates, and covariances of all three filters at time  $t_k$ .

**Step 1: Compute the Mixing Probabilities**

Given the model probabilities at time  $t_{k-1}$  and transition probabilities, compute the mixing probabilities

$$\mu_{k-1|k-1}^{ij} = \frac{1}{\bar{c}_j} \pi_{ij} \mu_{k-1}^i, \quad i, j = 1, 2, 3, \tag{78}$$

$$\bar{c}_j = \sum_{i=1}^3 \pi_{ij} \mu_{k-1}^i, \quad j = 1, 2, 3. \tag{79}$$

**Step 2: Compute the Mixed Initial States and Covariances**

Compute the mixed initial states and covariances,

$$\hat{\mathbf{x}}_{k-1|k-1}^{0,j} = \sum_{i=1}^3 \mu_{k-1|k-1}^{ij} \hat{\mathbf{x}}_{k-1|k-1}^i, \quad j = 1, 2, 3, \tag{80}$$

$$\mathbf{P}_{k-1|k-1}^{0,j} = \sum_{i=1}^3 \mu_{k-1|k-1}^{ij} \left[ \mathbf{P}_{k-1|k-1}^i + (\hat{\mathbf{x}}_{k-1|k-1}^i - \hat{\mathbf{x}}_{k-1|k-1}^{0,j})(\hat{\mathbf{x}}_{k-1|k-1}^i - \hat{\mathbf{x}}_{k-1|k-1}^{0,j})' \right], \quad j = 1, 2, 3. \tag{81}$$

**Step 3: Compute the Predicted State Estimates and Covariances**

The predicted state estimate and covariance for the NCV model are given, respectively, by

$$\hat{\mathbf{x}}_{k|k-1}^1 = \mathbf{F}_{k-1}^{(1)} \hat{\mathbf{x}}_{k-1|k-1}^{0,1}, \tag{82}$$

$$\mathbf{P}_{k|k-1}^1 = \mathbf{F}_{k-1}^{(1)} \mathbf{P}_{k-1|k-1}^{0,1} (\mathbf{F}_{k-1}^{(1)})' + \mathbf{Q}_{k-1}^{(1)}. \tag{83}$$

Since the NCT+ and NCT- models are nonlinear, the predicted state estimates and covariances are calculated by using cubature points. Thus, the predicted state estimates are given by

$$\hat{\mathbf{x}}_{k|k-1}^j = \sum_{i=1}^m w_i \mathbf{X}_{i,k|k-1}^{*,j}, \quad j = 2, 3. \tag{84}$$

where the  $i$ th predicted cubature point  $\mathbf{X}_{i,k|k-1}^{*,j}$  is calculated using (65)–(71). Then, the predicted covariances are calculated by

$$\mathbf{P}_{k|k-1}^j = \sum_{i=1}^m w_i \mathbf{X}_{i,k|k-1}^{*,j} (\mathbf{X}_{i,k|k-1}^{*,j})' - \hat{\mathbf{x}}_{k|k-1}^j (\hat{\mathbf{x}}_{k|k-1}^j)' + \mathbf{Q}_{k-1}^{(j)}, \quad j = 2, 3. \tag{85}$$

**Step 4: Compute the Innovation Covariance and Cross-covariance**

For all three models, the predicted measurement and innovation covariance are given, respectively, by

$$\hat{\mathbf{z}}_{k|k-1}^j = \sum_{i=1}^m w_i \mathbf{Z}_{i,k|k-1}^j, \quad j = 1, 2, 3. \tag{86}$$

$$\mathbf{P}_{\mathbf{z}\mathbf{z},k|k-1}^j = \sum_{i=1}^m w_i \mathbf{Z}_{i,k|k-1}^j (\mathbf{Z}_{i,k|k-1}^j)' - \hat{\mathbf{z}}_{k|k-1}^j (\hat{\mathbf{z}}_{k|k-1}^j)' + \mathbf{R}, \tag{87}$$

where  $\mathbf{Z}_{i,k|k-1}^j$  is calculated using (72)–(74). The cross-covariance is calculated by

$$\mathbf{P}_{\mathbf{x}\mathbf{z},k|k-1}^j = \sum_{i=1}^m w_i \mathbf{X}_{i,k|k-1}^j (\mathbf{Z}_{i,k|k-1}^j)' - \hat{\mathbf{x}}_{k|k-1}^j (\hat{\mathbf{z}}_{k|k-1}^j)'. \tag{88}$$

**Step 5: Compute the Model Likelihoods**

Calculate the model likelihoods by

$$\lambda_k^j = \mathcal{N}(v_k^j; \mathbf{0}, \mathbf{P}_{\mathbf{z}\mathbf{z},k|k-1}^j), \quad j = 1, 2, 3, \tag{89}$$

where  $v_k^j$  is the innovation and is given by

$$v_k^j = \mathbf{z}_k - \hat{\mathbf{z}}_{k|k-1}^j. \tag{90}$$

**Step 6: Compute the Updated States and Covariances**

$$\hat{\mathbf{x}}_{k|k}^j = \hat{\mathbf{x}}_{k|k-1}^j + \mathbf{K}_k^j v_k^j, \quad j = 1, 2, 3, \tag{91}$$

$$\mathbf{P}_{k|k}^j = \mathbf{P}_{k|k-1}^j - \mathbf{K}_k^j \mathbf{P}_{\mathbf{z}\mathbf{z},k|k-1}^j (\mathbf{K}_k^j)', \quad j = 1, 2, 3, \tag{92}$$

where the Kalman gain is given by

$$\mathbf{K}_k^j = \mathbf{P}_{\mathbf{x}\mathbf{z},k|k-1}^j (\mathbf{P}_{\mathbf{z}\mathbf{z},k|k-1}^j)^{-1}, \quad j = 1, 2, 3. \tag{93}$$

**Step 7: Update the Mode Probabilities**

Update the model probabilities by

$$\mu_k^j = \frac{1}{c} \lambda_k^j \bar{c}_j, \quad j = 1, 2, 3. \tag{94}$$

**Step 8: Compute the Combined State Estimate and Covariance**



The combined state estimate and covariance are given, respectively, by

$$\hat{\mathbf{x}}_{k|k} = \sum_{j=1}^3 \mu_k^j \hat{\mathbf{x}}_{k|k}^j \tag{95}$$

$$\mathbf{P}_{k|k} = \sum_{j=1}^3 \mu_k^j \left[ \mathbf{P}_{k|k}^j + \left( \hat{\mathbf{x}}_{k|k}^j - \hat{\mathbf{x}}_{k|k} \right) \left( \hat{\mathbf{x}}_{k|k}^j - \hat{\mathbf{x}}_{k|k} \right)' \right]. \tag{96}$$

A schematic diagram of the IMM filter based on the CKF is shown in Figure 4.

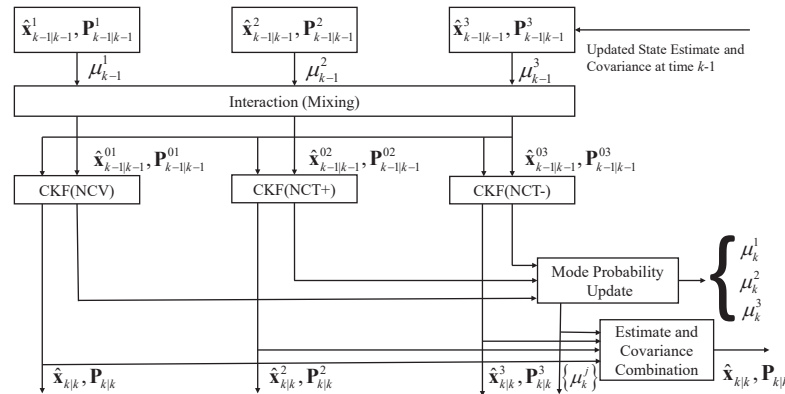


Figure 4. The IMM filter based on CKF.

A large number of publications using the IMM estimator are available in the literature. A few selected relevant papers are discussed based on their technical contribution and results. Li and Bar-Shalom [29] considered a maneuvering aircraft in the air traffic control (ATC) problem with accelerations of 0.6g, 1g, and 2g. The measurements of the ATC radar are range and azimuth, which were converted to unbiased Cartesian position measurements. They used two versions of the IMM-EKF with the NCV and NCT motions. Kastella and Biscuso [30] performed an extensive study on the ATC problem and showed that the IMM-EKF with the NCV and NCT motions had superior performance over the adaptive single model KF. The maximum acceleration for the high-performance turn was 3.3g. Generic maneuvering aircraft with accelerations of 1g, 1.5g, 2.5g, and 3g were studied in [31] using radar range, azimuth, and range rate measurements. The authors used the EKF-based switching grid and adaptive grid IMM filters. Blackman et al. [32] analyzed a highly maneuvering aircraft with a maximum acceleration of 3g using the NCT motion.

### 8. Posterior Cramér-Rao Lower Bound (PCRLB)

Consider the discrete-time dynamic and measurement models given, respectively, by

$$\mathbf{x}_k = \mathbf{f}_{k-1}(\mathbf{x}_{k-1}, \mathbf{w}_{k-1}), \tag{97}$$

$$\mathbf{z}_k = \mathbf{h}_k(\mathbf{x}_k, \mathbf{n}_k). \tag{98}$$

Let  $\hat{\mathbf{x}}_{k|k}$  be an unbiased estimator of the state vector  $\mathbf{x}_k$ , based on measurement sequence  $\mathbf{Z}_k = \{\mathbf{z}_1, \dots, \mathbf{z}_k\}$  and prior density  $p(\mathbf{x}_0)$ . Then, the mean square error matrix (MSEM) of  $\hat{\mathbf{x}}_{k|k}$ , denoted as  $\Sigma_{k|k}$ , has a lower bound, called the PCRLB  $\mathbf{J}_k^{-1}$  [5,20,59–61]:

$$\Sigma_{k|k} := E\{(\hat{\mathbf{x}}_{k|k} - \mathbf{x}_k)(\hat{\mathbf{x}}_{k|k} - \mathbf{x}_k)'\} \geq \mathbf{J}_k^{-1}, \tag{99}$$

where  $\mathbf{J}_k$  represents the Bayesian information matrix [20]. Tichavsky et al. [60] derived an elegant recursive expression to compute  $\mathbf{J}_k$  recursively by using

$$\mathbf{J}_k = \mathbf{D}_{k-1}^{33} - (\mathbf{D}_{k-1}^{12})' (\mathbf{J}_{k-1} + \mathbf{D}_{k-1}^{11})^{-1} \mathbf{D}_{k-1}^{12} + \mathbf{J}_{k,Z}, \tag{100}$$

where, for additive Gaussian process noise and measurement noise (valid for our current problem) [5,20,61],

$$\mathbf{D}_{k-1}^{11} = E\{\bar{\mathbf{F}}'_{k-1} \mathbf{Q}_{k-1}^{-1} \bar{\mathbf{F}}_{k-1}\}, \tag{101}$$

$$\bar{\mathbf{F}}_{k-1} = [\nabla_{\mathbf{x}_{k-1}} \mathbf{f}'_{k-1}(\mathbf{x}_{k-1})]', \tag{102}$$

$$\mathbf{D}_{k-1}^{12} = -E\{\bar{\mathbf{F}}'_{k-1}\} \mathbf{Q}_{k-1}^{-1}, \tag{103}$$

$$\mathbf{D}_{k-1}^{33} = \mathbf{Q}_{k-1}^{-1}, \tag{104}$$

$$\mathbf{J}_{k,Z} = E\{\bar{\mathbf{H}}'_k \mathbf{R}_k^{-1} \bar{\mathbf{H}}_k\}, \tag{105}$$

$$\bar{\mathbf{H}}_k = [\nabla_{\mathbf{x}_k} \mathbf{h}'_k(\mathbf{x}_k)]'. \tag{106}$$

The Jacobian matrices  $\bar{\mathbf{F}}_{k-1}$  in (102) and  $\bar{\mathbf{H}}_k$  in (106) are nonlinear functions of the true states. Therefore, it is not possible to calculate the expected values in equations (101), (103), and (105) by using analytical methods. We evaluated these expected values using Monte Carlo runs. For the NCV motion,

$$\mathbf{D}_{k-1}^{11} = (\mathbf{F}_{k-1}^1)' \mathbf{Q}_{k-1}^{-1} \mathbf{F}_{k-1}^1, \tag{107}$$

$$\mathbf{D}_{k-1}^{12} = -\mathbf{F}'_{k-1} \mathbf{Q}_{k-1}^{-1}. \tag{108}$$

A detailed derivation of the Jacobian  $\bar{\mathbf{F}}_k$  for the time evolution function is presented in Appendix A. A detailed derivation of the Jacobian  $\bar{\mathbf{H}}_k$  for the AMTI measurement function is presented in Appendix B and is given by

$$\bar{\mathbf{H}}_k = \begin{bmatrix} \mathbf{u}'_k & \mathbf{0}_{1 \times 2} \\ \frac{u_{y,k}}{r_k} & -\frac{u_{x,k}}{r_k} & \mathbf{0}_{1 \times 2} \\ \frac{\mathbf{v}'_k}{r_k} [\mathbf{I}_2 - \mathbf{u}_k \mathbf{u}'_k] & \mathbf{u}'_k \end{bmatrix} \tag{109}$$

### 9. Measures of Performance (MoP)

In order to evaluate the performance of the IMM-EKF, IMM-UKF, and IMM-CKF filters, we calculate the RMS position and velocity errors, ANEES [8,24,62,63], RTAMS errors [12,18,51,63], covariance consistency metric, and CPU times using Monte Carlo simulation. Given the true state  $\mathbf{x}_{k,i}$  and estimated state  $\hat{\mathbf{x}}_{k|k,i}$  of the aircraft, the RMS position and velocity errors at time  $t_k$  are defined, respectively, by

$$\text{RMS}_{\text{position},k} = \sqrt{\frac{1}{M} \sum_{i=1}^M [(x_{k,i} - \hat{x}_{k|k,i})^2 + (y_{k,i} - \hat{y}_{k|k,i})^2]}, \tag{110}$$

$$\text{RMS}_{\text{velocity},k} = \sqrt{\frac{1}{M} \sum_{i=1}^M [(\dot{x}_{k,i} - \hat{\dot{x}}_{k|k,i})^2 + (\dot{y}_{k,i} - \hat{\dot{y}}_{k|k,i})^2]}, \tag{111}$$

where  $M$  denotes the number of Monte Carlo runs.

The root time-averaged mean square (RTAMS) position and velocity errors [5,20,52] are defined, respectively, by

$$\text{RTAMS}_{\text{position}} = \sqrt{\frac{1}{(k_2 - k_1 + 1)M} \sum_{k=k_1}^{k_2} \sum_{i=1}^M [(x_{k,i} - \hat{x}_{k|k,i})^2 + (y_{k,i} - \hat{y}_{k|k,i})^2]}, \tag{112}$$

$$\text{RTAMS}_{\text{velocity}} = \sqrt{\frac{1}{(k_2 - k_1 + 1)M} \sum_{k=k_1}^{k_2} \sum_{i=1}^M [(\dot{x}_{k,i} - \hat{\dot{x}}_{k|k,i})^2 + (\dot{y}_{k,i} - \hat{\dot{y}}_{k|k,i})^2]}, \tag{113}$$

where  $k_1$  and  $k_2$  are the first and the last indices of the trajectory segment, respectively.

At time  $t_k$ , the ANEES is calculated as [8,24,62,63]

$$\text{ANEES}_k := \frac{1}{nM} \sum_{i=1}^M (\mathbf{x}_{k,i} - \hat{\mathbf{x}}_{k|i,i})' \mathbf{P}_{k|i,i}^{-1} (\mathbf{x}_{k,i} - \hat{\mathbf{x}}_{k|i,i}), \tag{114}$$

where  $n$  denotes the dimension of the state, and  $\mathbf{P}_{k|i,i}$  is the covariance corresponding to  $\hat{\mathbf{x}}_{k|i,i}$ . The criterion for determining that the estimation error is consistent with the calculated covariance of the filter at time  $t_k$  is that  $\text{ANEES}_k$  lies within the two-sided 99% confidence interval. For 1,000 Monte Carlo runs and a four-dimensional state vector, the 99% confidence interval is [0.943, 1.058]. Since the nonlinear filters are approximate, the filter calculated covariance, in general, is different from the actual mean square error matrix (MSEM). The average of the covariance matrix at time  $t_k$  is  $\bar{\mathbf{P}}_{k|k} = \frac{1}{M} \sum_{i=1}^M \mathbf{P}_{k|i,i}$ . The MSEM at time  $t_k$  is specified by

$$\text{MSEM}_k = \frac{1}{M} \sum_{i=1}^M (\mathbf{x}_{k,i} - \hat{\mathbf{x}}_{k|i,i})(\mathbf{x}_{k,i} - \hat{\mathbf{x}}_{k|i,i})'. \tag{115}$$

At time  $t_k$ , to determine the covariance consistency of a filter, we compute the ratio

$$\zeta_k = \frac{\text{trace}(\bar{\mathbf{P}}_{k|k})}{\text{trace}(\text{MSEM}_k)}. \tag{116}$$

If  $\zeta_k$  is close to unity, then the filter-calculated covariance is a good measure of the MSEM. Thus,  $\zeta_k$  can be regarded as a second metric for covariance consistency.

### 10. Numerical Simulations and Results

In this study, the motion patterns of a highly maneuvering aircraft are the same as the target’s motion patterns in [64,65], which are NCV, NCT+, NCV, NCT-, and NCV in sequence. In the experiments considered in this section, the acceleration of the target during the NCT+ and NCT- phases is 3g, 4g, 5g, and 6g, respectively, while only the case with an acceleration of 4g was considered in [64]. The prior distribution of the aircraft’s state and the power spectral densities (PSDs) of the process noise during the NCV and NCT phases are the same as in reference [64], as shown in Table 2. The impact of prior covariance on filtering accuracy was studied further in [65]. The AMTI radar moves with constant velocity in 2D along the X-axis and measures the range, azimuth, and radial velocity of the aircraft. The initial position and velocity of the sensor and measurement parameters are shown in Table 3. In the IMM filters, we use a constant transition probability matrix [8], which is given by

$$\mathbf{\Pi} = \begin{bmatrix} 0.95 & 0.025 & 0.025 \\ 0.04 & 0.95 & 0.01 \\ 0.04 & 0.01 & 0.95 \end{bmatrix}. \tag{117}$$

We used 1000 Monte Carlo runs to compute the various MoPs of the IMM-based filters. We analyze the MoP of the filters using three azimuth SDs of 1, 2, 4 mrad and two measurement time intervals of 0.5 and 1.0 s. For filter initialization, we draw a sample from the prior distribution in each Monte Carlo run and set it to the initial state estimate. Therefore, the initial state estimate is different from the true initial state in each Monte Carlo run.

**Table 2.** Aircraft parameters.

Variable	Value
Prior mean position	(1000, 20,000) m
Prior mean velocity	(374.332, 0) m/s
Variance of prior position	$(40^2, 40^2)$ m <sup>2</sup>
Variance of prior velocity	$(4^2, 4^2)$ (m/s) <sup>2</sup>
NCV: PSD of process noise ( $q_1$ )	0.1 m <sup>2</sup> /s <sup>3</sup>
NCT: PSD of process noise ( $q_2$ )	0.01 m <sup>2</sup> /s <sup>3</sup>

**Table 3.** Sensor parameters.

Variable	Value
Initial position	(−11,500, 5000) m
Constant velocity	(200, 0) m/s
Range SD	10 m
Azimuth SD	1, 2, 4 mrad
Radial velocity SD	1 m/s
Measurement time interval ( $T$ )	0.5, 1.0 s
Number of measurements ( $N$ )	481, 241

We present the numerical results in Sections 10.1–10.3 with varying parameters.

10.1. Numerical Results for  $T = 0.5$  s

The RMS position and velocity errors for the IMM-EKF, IMM-UKF, IMM-CKF, and PCRLB in 3g, 4g, 5g, and 6g cases are presented in Figures 5 and 6, respectively. In Figures 5 and 6, we observe that the RMS position and velocity errors from various filters are nearly the same. In order to understand the results in Figures 5 and 6, we have presented the time indices of dynamic models in Table 4. From Figures 5 and 6, it is noted that the RMS errors in position and velocity during the NCV phases approximate the respective PCRLB values closely. Nonetheless, minor discrepancies exist between the RMS errors and their corresponding PCRLB values within the NCT+ and NCT- phases.

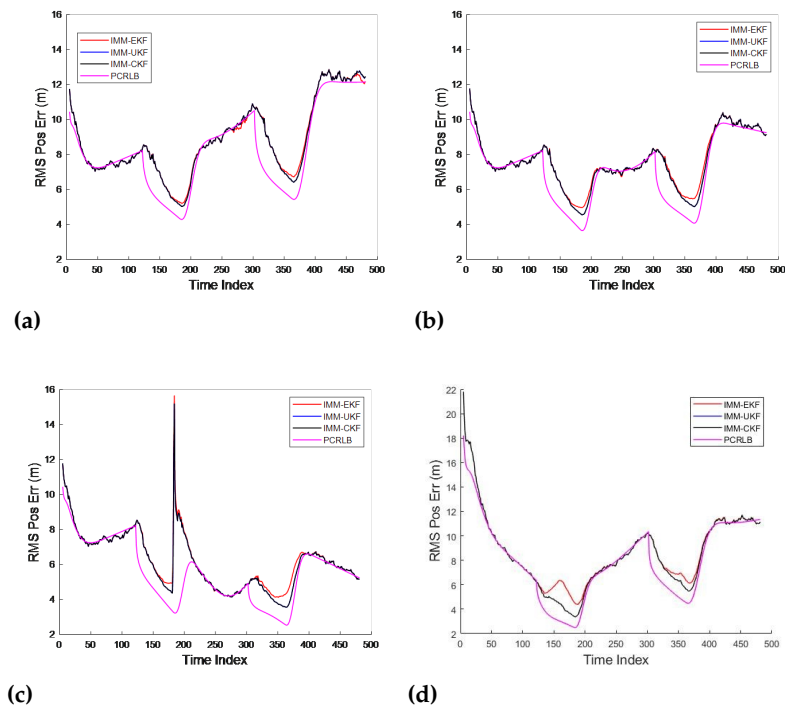


**Figure 5.** RMS position error in (a) 3g, (b) 4g, (c) 5g, and (d) 6g cases for  $T = 0.5$  s.

**Table 4.** Time indices of dynamic models for  $T = 0.5$  s.

Time Indices	Dynamic Model
1–121	NCV
121–181	NCT+
181–301	NCV
301–361	NCT-
361–481	NCV

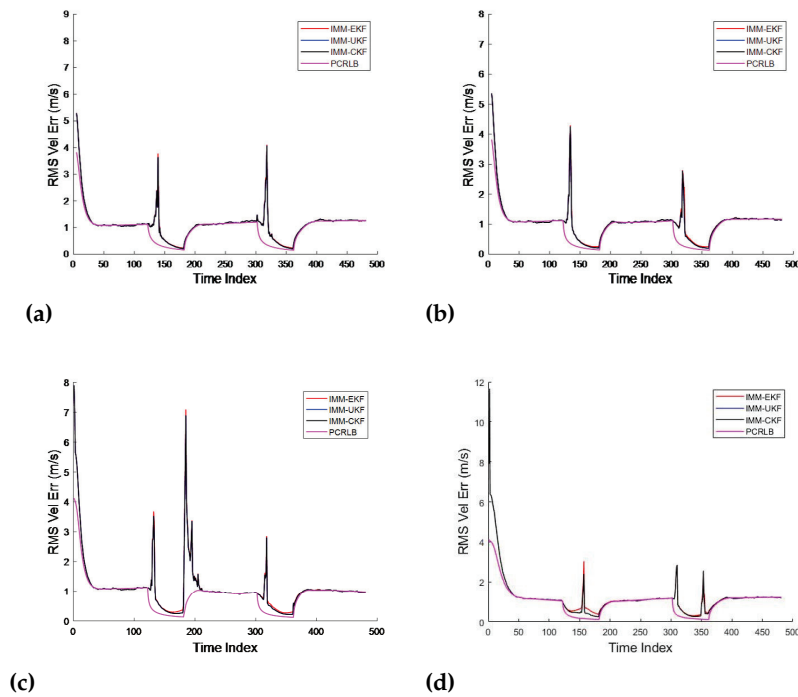


**Figure 6.** RMS position error in (a) 3g, (b) 4g, (c) 5g, and (d) 6g cases for  $T = 0.5$  s.

In order to see the differences in the RMS errors of various filters, we have plotted the RMS position and velocity differences (EKF-UKF) and (EKF-CKF) in Figures 7a and 7b, respectively. Figure 7 illustrates that the IMM-UKF and IMM-CKF filters demonstrate a comparable level of precision, and they both marginally outperform the IMM-EKF in terms of accuracy. The spikes in differences occur during the NCT+ and NCT- segments.

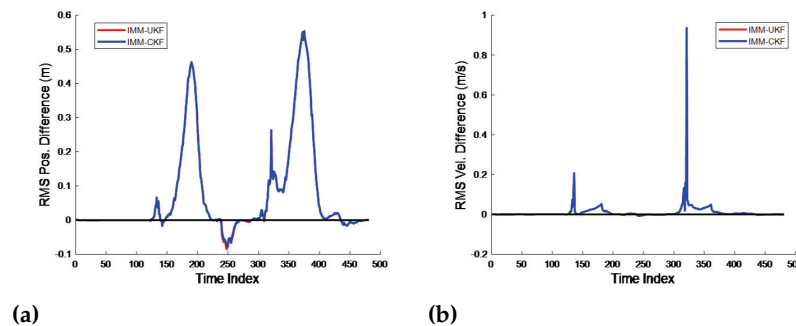


**Figure 7.** (a) RMS position difference; (b) RMS velocity difference for 4g, azimuth SD = 1 mrad, and  $T = 0.5$  s.

Figure 8 displays the ANEES for the three IMM filters under consideration across three distinct acceleration scenarios, all bounded by the 99% confidence intervals. It is evident from the figure that the ANEES remains within the 99% confidence limits for segments

where the aircraft’s motion is characterized by NCV. Conversely, for the NCT segments, the ANEES is observed to exceed these limits. This discrepancy suggests that while the filters’ computed covariance matrices align well with the estimation errors during the NCV phases, they fail to maintain the same consistency during the NCT+ and NCT- phases. Further research is warranted to address this issue and enhance the covariance calculations within the NCT segments for improved filtering performance. A magnified view of ANEES for the 4g case is shown in Figure 9a, and the covariance consistency metric  $\zeta_k$  is plotted in Figure 9b. The plot of  $\zeta_k$  in Figure 9b indicates that the IMM-UKF and IMM-CKF-calculated covariances have better covariance consistency than that of the IMM-EKF.

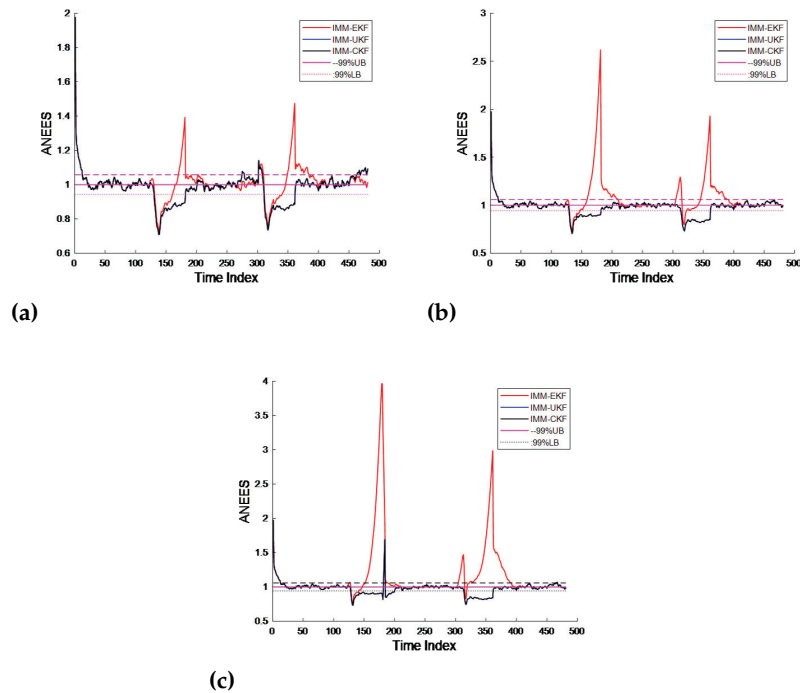


Figure 8. ANEES in (a) 3g, (b) 4g, and (c) 5g cases for  $T = 0.5$  s.

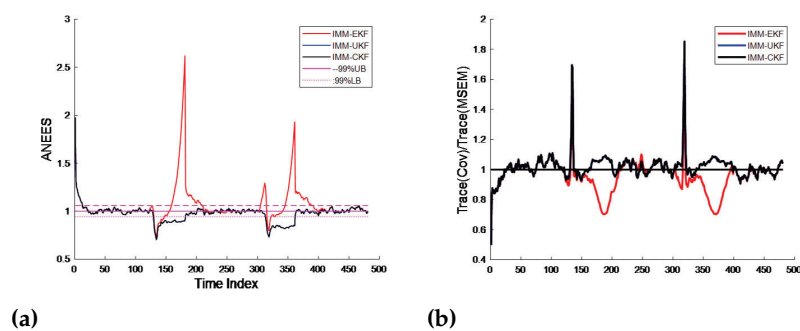


Figure 9. (a) ANEES; (b) Trace (Cov)/Trace (MSEM) for 4g, azimuth SD = 1 mrad, and  $T = 0.5$  s.

In the first Monte Carlo run, Figure 10 depicts the mode probabilities for the 3g, 4g, and 5g cases for the IMM-CKF. When comparing the mode probabilities in Figure 10 with the results in Table 3, we find that the mode probabilities for the first NCV, NCT+, second NCV, NCT-, and third NCV segments are calculated accurately. Moreover, the mode probabilities approach a value of one in most cases. A similar trend is observed for the IMM-EKF and IMM-UKF.

Table 5 presents the RTAMS position and velocity errors and corresponding PCRLBs for the NCT- and last NCV segment. The results in Table 5 show that the RTAMS position and velocity errors of the IMM-UKF and IMM-CKF are nearly the same, and those of the



IMM-EKF are slightly higher. In the final NCV phase, the RTAMS errors of the three IMM filters nearly approximate their respective PCRLB values. Conversely, during the segment involving the NCT-, the discrepancies between the RTAMS errors recorded by the IMM filters and the corresponding PCRLB values are somewhat higher.

From Figure 2, we observe that the trajectories of the aircraft are different in the three acceleration cases. Therefore, we cannot compare the accuracies of the filtering results among the three scenarios.

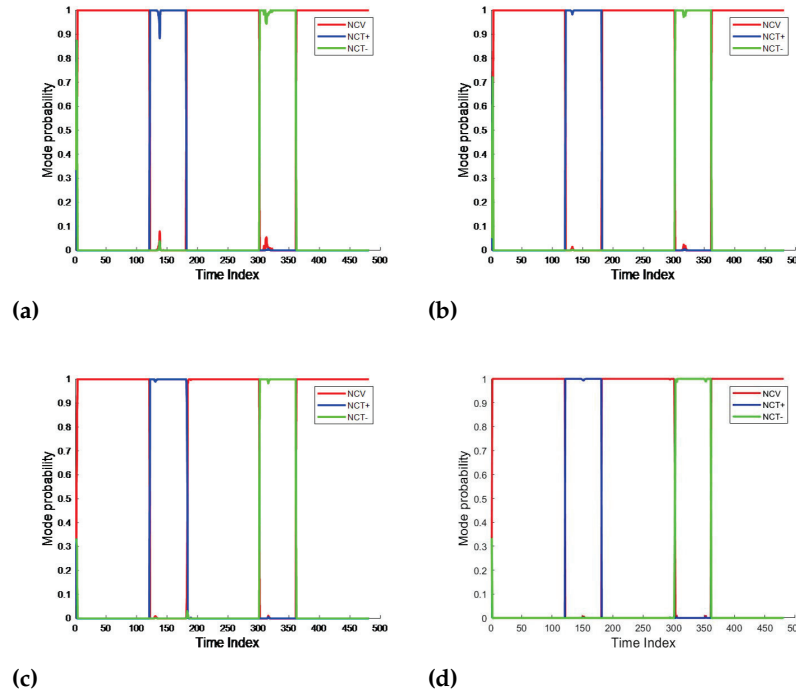


Figure 10. Mode probabilities for (a) 3g, (b) 4g, (c) 5g, and (d) 6g cases for the IMM-CKF for  $T = 0.5$  s.

Table 5. RTAMS errors for  $T = 0.5$  s.

Acceleration	Segment	RTAMS Error	IMM-EKF	IMM-UKF	IMM-CKF	PCRLB
3g	NCT-	Position (m)	8.663	8.616	8.615	6.871
		Velocity (m/s)	1.105	1.084	1.083	0.407
	Last NCV	Position (m)	11.288	11.273	11.278	10.848
		Velocity (m/s)	1.193	1.192	1.192	1.175
4g	NCT-	Position (m)	6.809	6.694	6.694	5.225
		Velocity (m/s)	0.925	0.859	0.859	0.349
	Last NCV	Position (m)	9.076	8.986	8.986	8.712
		Velocity (m/s)	1.123	1.120	1.120	1.106
5g	NCT-	Position (m)	4.689	4.470	4.470	3.330
		Velocity (m/s)	0.740	0.701	0.701	0.298
	Last NCV	Position (m)	5.985	5.845	5.845	5.655
		Velocity (m/s)	0.995	0.990	0.990	0.978

We present the CPU times required for each execution of the Monte Carlo simulation in Table 6. The results in Table 6 indicate that the IMM-EKF completes the run in the least amount of CPU time. In comparison, the CPU time for both the IMM-UKF and IMM-CKF is approximately 1.6 times the CPU time of the IMM-EKF. Additionally, the IMM-CKF

slightly outperforms the IMM-UKF in terms of CPU time, consuming a marginally smaller CPU time. This is due to the fact that the CKF uses  $2n$  cubature points, whereas the UKF uses  $2n + 1$  sigma points.

10.2. Comparison of IMM-CKF MoP with Varying Azimuth SD with  $T = 0.5$  s

Since all IMM-based filters have nearly the same state estimation accuracy, we use the IMM-CKF for this comparison. In Figures 11 and 12, the RMS position and velocity errors for three different values of azimuth error SDs using the IMM-CKF and corresponding PCRLBs are plotted. It is observed that as the azimuth error SD increases, the RMS position and velocity errors and PCRLBs also increase. The same trend can be observed in Table 7, which presents the RTAMS position and velocity errors and corresponding PCRLBs for all three cases of azimuth error SDs. The velocity RMS error and corresponding PCRLB are nearly the same for all three azimuth error SDs. As the azimuth error SD increases, the difference between the RTAMS position error and corresponding PCRLB increases slightly.

Table 6. CPU times per Monte Carlo run for  $T = 0.5$  s.

Case	CPU Time	IMM-EKF	IMM-UKF	IMM-CKF
3g	Absolute (s)	0.273	0.440	0.417
	Relative	1.000	1.612	1.527
4g	Absolute (s)	0.293	0.456	0.433
	Relative	1.000	1.670	1.586
5g	Absolute (s)	0.370	0.611	0.578
	Relative	1.000	1.651	1.562

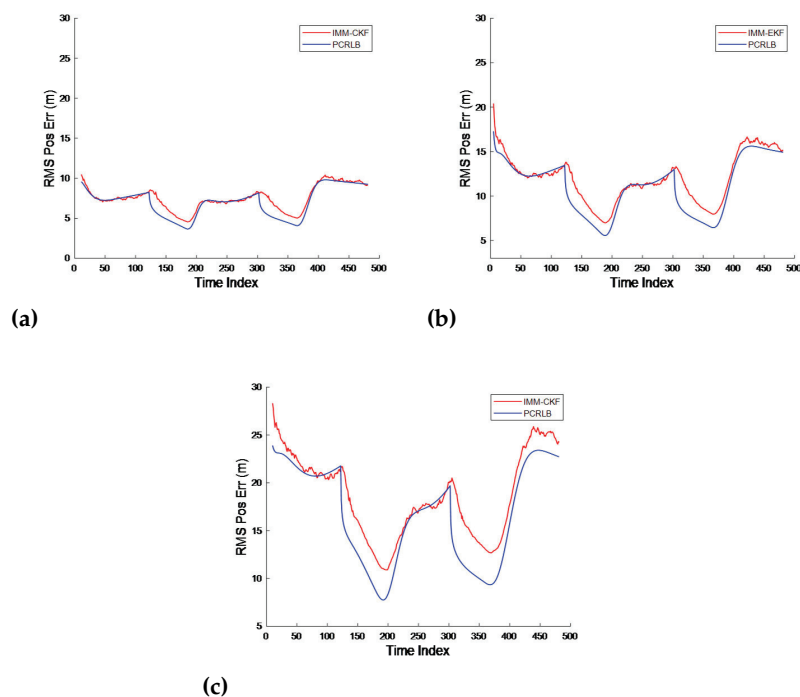
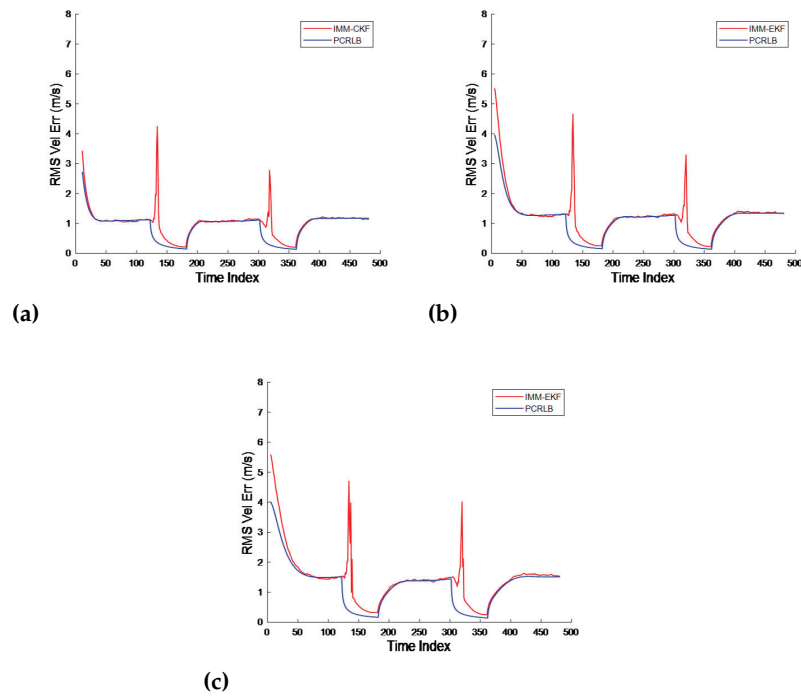


Figure 11. RMS position errors for (a) 1 mrad, (b) 2 mrad, and (c) 4 mrad azimuth error SD in the 4g case.



**Figure 12.** RMS velocity errors for (a) 1 mrad, (b) 2 mrad, and (c) 4 mrad azimuth error SD in the 4g case.

**Table 7.** RTAMS errors for 4g using IMM-CKF and PCRLB for  $T = 0.5$  s.

Azimuth SD	Segment	RTAMS Error	IMM-EKF	IMM-UKF	IMM-CKF	PCRLB
1 mrad	NCT-	Position (m)	6.809	6.694	6.694	5.225
		Velocity (m/s)	0.925	0.859	0.859	0.341
	Last NCV	Position (m)	9.076	8.986	8.986	8.712
		Velocity (m/s)	1.123	1.120	1.120	1.106
2 mrad	NCT-	Position (m)	4.689	4.470	4.470	3.330
		Velocity (m/s)	0.740	0.701	0.701	0.298
	Last NCV	Position (m)	5.985	5.845	5.845	5.655
		Velocity (m/s)	0.995	0.990	0.990	0.978
4 mrad	NCT-	Position (m)	16.265	16.118	16.119	11.676
		Velocity (m/s)	1.464	1.184	1.184	0.401
	Last NCV	Position (m)	21.531	21.234	21.236	19.219
		Velocity (m/s)	1.436	1.430	1.423	1.374

10.3. Comparison of IMM-CKF MoP with Varying Measurement Time Interval

Figures 13 and 14 present the RMS position and velocity errors in the 4g case with the measurement time intervals of 0.5 s and 1 s using the IMM-CKF. We observe that as the measurement time interval increases, the RMS position and velocity errors also increase, as expected. This can also be observed from Table 8, which shows the RTAMS errors for both position and velocity.

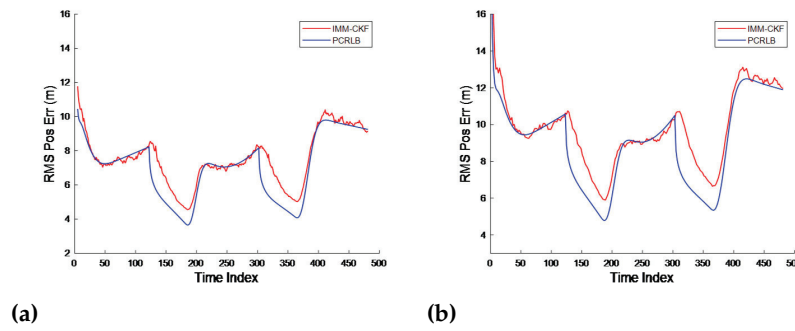


Figure 13. RMS position errors for the 4g case using (a)  $T = 0.5$  s and (b)  $T = 1$  s.

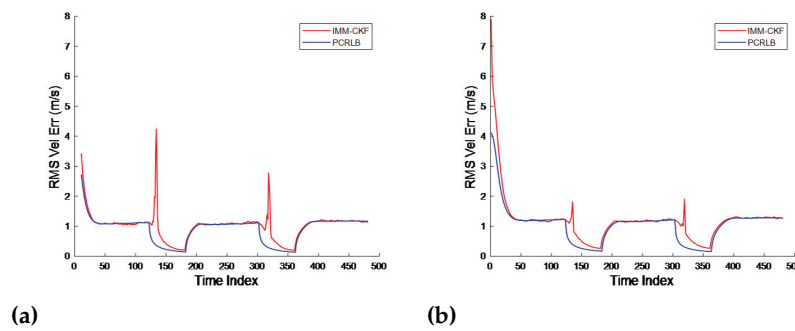


Figure 14. RMS velocity errors for the 4g case using (a)  $T = 0.5$  s and (b)  $T = 1$  s.

10.4. Comparison of Algorithms with Low Measurement Accuracy and Low Data Rate

In previous cases, realistic measurement SDs and measurement time intervals were used. As a result, the state estimation accuracies of the various IMM filters are nearly the same. In order to evaluate the performance of the IMM filters with high SDs and measurement time intervals, the accuracy of state estimation among the three IMM filters is quite similar. In order to evaluate the performance of the various IMM filters with high SDs and measurement time intervals, we used  $\sigma_r = 50$  m,  $\sigma_\beta = 5^\circ$ ,  $\sigma_{v_r} = 5$  m/s, and  $T = 2.0$  s. Table 9 presents the measurement time indices of various dynamic models. The RTAMS position and velocity errors for the NCT- and last NCV segment are presented in Table 10. The results in Table 10 show that the IMM-CKF and IMM-EKF have the best and the worst performances, respectively, and the performance of the IMM-UKF is close to that of the IMM-CKF. The RMS position and velocity errors are presented in Figure 15. Figure 16a,b show the ANEES and  $\zeta_k = \text{Trace}(\text{Cov})/\text{Trace}(\text{MSEM})$ . The above findings indicate that the IMM-UKF and IMM-CKF have better covariance consistency than the IMM-EKF.

Table 8. RTAMS errors for IMM-CKF and PCRLB for 4g using  $T = 0.5$  s and 1.0 s.

Time Interval	Segment	RTAMS Error	IMM-EKF	IMM-UKF	IMM-CKF	PCRLB
0.5 s	NCT-	Position (m)	6.809	6.694	6.694	5.225
		Velocity (m/s)	0.925	0.859	0.859	0.341
	Last NCV	Position (m)	9.076	8.986	8.986	8.712
		Velocity (m/s)	1.123	1.120	1.120	1.106
1.0 s	NCT-	Position (m)	8.958	8.779	8.779	7.141
		Velocity (m/s)	0.905	0.831	0.831	0.432
	Last NCV	Position (m)	11.494	11.370	11.370	10.944
		Velocity (m/s)	1.222	1.216	1.216	1.191

**Table 9.** Time indices of dynamic models for  $T = 2.0$  s.

Time Indices	Dynamic Model
1–31	NCV
31–46	NCT+
46–76	NCV
76–91	NCT-
91–121	NCV

**Table 10.** RTAMS errors with  $\sigma_r = 50$  m,  $\sigma_\beta = 5^\circ$ ,  $\sigma_{v_r} = 5$  m/s, and  $T = 2.0$  s.

Segment	RTAMS Error	IMM-EKF	IMM-UKF	IMM-CKF	PCRLB
NCT-	Position (m)	146.341	127.031	126.935	47.459
	Velocity (m/s)	6.376	3.572	3.568	1.105
Last NCV	Position (m)	170.592	122.847	122.193	54.900
	Velocity (m/s)	2.761	2.328	2.327	2.012

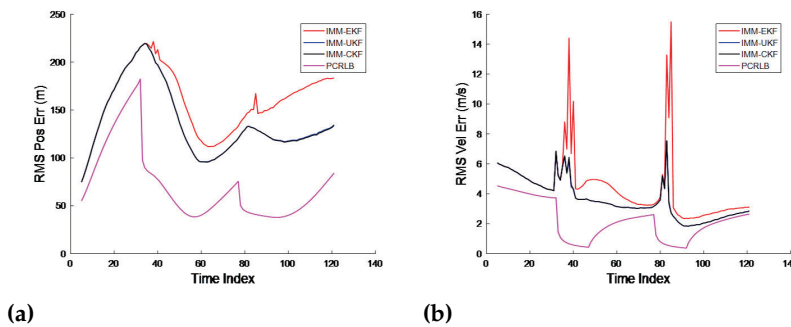


**Figure 15.** RMS (a) position and (b) velocity errors for  $4g$ ,  $\sigma_r = 50$  m,  $\sigma_\beta = 5^\circ$ ,  $\sigma_{v_r} = 5$  m/s, and  $T = 2.0$  s.

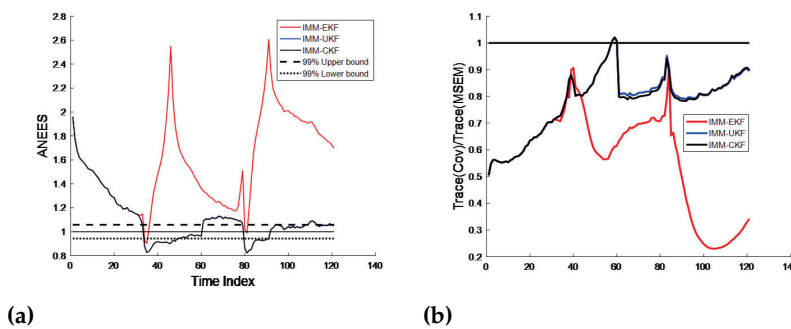


**Figure 16.** (a) ANEES; (b)  $\zeta_k = \text{Trace}(\text{Cov})/\text{Trace}(\text{MSEM})$  for  $4g$ ,  $\sigma_r = 50$  m,  $\sigma_\beta = 5^\circ$ ,  $\sigma_{v_r} = 5$  m/s, and  $T = 2.0$  s.

We kept all the parameters the same and used  $\sigma_\beta = 1^\circ$  to examine the RTAMS errors for both position and velocity in the IMM filters, thereby highlighting their performance variations. Table 11 presents the resulting RTAMS position and velocity errors. The results in Tables 10 and 11 show that as the measurement accuracy increases, the performance of the IMM-EKF approaches those of the IMM-UKF or IMM-CKF.

**Table 11.** RTAMS errors with  $\sigma_r = 50$  m,  $\sigma_\beta = 1^\circ$ ,  $\sigma_{v_r} = 5$  m/s, and  $T = 2.0$  s.

Segment	RTAMS Error	IMM-EKF	IMM-UKF	IMM-CKF	PCRLB
NCT-	Position (m)	83.04	81.497	81.41	1.07
	Velocity (m/s)	3.75	2.869	2.86	1.10
Last NCV	Position (m)	102.71	78.278	78.24	51.72
	Velocity (m/s)	2.51	2.230	2.23	1.99

## 11. Conclusions

In this study, we offer a comprehensive review of IMM filtering techniques specifically applied to the tracking of a highly maneuvering aircraft that is being monitored by an AMTI radar system situated on a separate aircraft. Single-model filtering and hybrid state-estimation algorithms are first described, and then the dynamic and measurement models associated with the problem are explained. We summarize the EKF, UKF, and CKF used in the IMM estimator and present detailed steps for the IMM-CKF. In order to compare the state estimation accuracies of the IMM-EKF, IMM-UKF, and IMM-CKF, we give a derivation of the PCRLB. Finally, we analyze the performance of various IMM-based filtering algorithms.

The aircraft has a range of accelerations, specifically 3g, 4g, 5g, and 6g. We used the RMS errors in position and velocity, ANEES, a covariance consistency metric, PCRLB, model probabilities, and computational cost as performance metrics to compare the performances of the three IMM-based filters. We also compared the root RTAMS errors of position and velocity and the associated CPU times. Our results show that for the operational measurement accuracy of the AMTI radar (range SD = 10 m; azimuth SD = 1, 2, and 4 mrad; radial velocity SD = 1 m/s), the performances of these three filters are nearly the same for  $T = 0.5$  s. The RMS position and velocity errors are close to the corresponding PCRLB values in the NCV segments, but small differences occur in the NCT segments. The ANEES remains confined within the 99% confidence intervals during the NCV phases, whereas it exceeds these intervals in the NCT phases. The results on mode probabilities show that the three IMM-based filters are able to select the correct dynamic model for various segments of the aircraft trajectory. The RTAMS errors of position and velocity are nearly the same for these three IMM-based filters, and they are slightly higher than the corresponding PCRLB values. The IMM-EKF exhibits the shortest CPU time, with the IMM-UKF and IMM-CKF requiring approximately 1.6 times more CPU time in comparison.

We also analyze the performance of these three IMM filters at significantly higher measurement SDs and  $T = 2$  s for the 4g aircraft. In this case, the performance of the IMM-UKF and IMM-CKF is essentially comparable, whereas the IMM-EKF performs the least effectively among the three. This classical trend of the EKF, UKF, and CKF occurs at much higher SDs, which is outside the operational domain of the AMTI radar.

We study the performance of the IMM-CKF by varying the azimuth SD with values of 1, 2, and 4 mrad, with a measurement time interval of 0.5 s. We observe that the RMS position and velocity errors and the RTAMS position and velocity errors are close to the corresponding PCRLB values. The performance of the IMM-CKF gracefully degrades as the azimuth SD increases. We also studied the performance of the IMM-CKF by using measurement time intervals of 0.5 and 1.0 s. In both cases, the RMS errors in position and velocity, as well as the RTAMS errors for position and velocity, were found to be in close proximity to their respective PCRLB values.

Our future work will consider scenarios where the target aircraft and AMTI aircraft move in 3D space. We shall also focus on using improved NCT models and new algorithms for a maneuvering target [66].



**Author Contributions:** Conceptualization, M.M., M.N.R. and X.T.; methodology, M.M., M.N.R. and X.T.; software, M.N.R. and M.M; validation, M.M., M.N.R. and X.T.; writing—original draft preparation, M.N.R., M.M. and X.T.; writing—review and editing, M.M., M.N.R. and X.T. All authors have read and agreed to the published version of the manuscript.

**Funding:** This research received no external funding.

**Data Availability Statement:** No new data were created or analyzed in this study. Data sharing is not applicable to this article.

**Conflicts of Interest:** The authors declare no conflicts of interest.

### Appendix A

This appendix presents the detailed derivation of the time evolution function with respect to the state vector. Given the nonlinear dynamic models for the NCT motions (31) and (32),

$$\mathbf{x}_k = \mathbf{A}^{(j)}(\mathbf{x}_{k-1})\mathbf{x}_{k-1} + \mathbf{w}_{k-1}^{(j)}, \quad j = 2, 3, \tag{A1}$$

For simplicity, we drop the superscript  $j$  in (A1). Then, from (33), we have

$$\mathbf{A}(\mathbf{x}_{k-1}) = \begin{bmatrix} 1 & 0 & \frac{\sin(\omega T)}{\omega} & -\frac{1-\cos(\omega T)}{\omega} \\ 0 & 1 & \frac{1-\cos(\omega T)}{\omega} & \frac{\sin(\omega T)}{\omega} \\ 0 & 0 & \cos(\omega T) & -\sin(\omega T) \\ 0 & 0 & \sin(\omega T) & \cos(\omega T) \end{bmatrix}, \tag{A2}$$

$$\omega = \frac{\kappa a_m}{\sqrt{\dot{x}_{k-1}^2 + \dot{y}_{k-1}^2}}. \tag{A3}$$

Define

$$\eta_1 := \sin \omega T, \tag{A4}$$

$$\eta_2 := \cos \omega T, \tag{A5}$$

$$\eta_3 := \frac{\sin \omega T}{\omega} = \frac{\eta_1}{\omega} \tag{A6}$$

$$\eta_4 := \frac{1 - \cos \omega T}{\omega} = \frac{1 - \eta_2}{\omega}. \tag{A7}$$

Then, from (32), we obtain

$$\mathbf{f}(\mathbf{x}_{k-1}) = \mathbf{A}(\mathbf{x}_{k-1})\mathbf{x}_{k-1}, \tag{A8}$$

where

$$\mathbf{f}(\mathbf{x}_{k-1}) = \mathbf{A}(\mathbf{x}_{k-1})\mathbf{x}_{k-1} = \begin{bmatrix} \mathbf{a}'_1 \mathbf{x}_{k-1} \\ \mathbf{a}'_2 \mathbf{x}_{k-1} \\ \mathbf{a}'_3 \mathbf{x}_{k-1} \\ \mathbf{a}'_4 \mathbf{x}_{k-1} \end{bmatrix} = \begin{bmatrix} f_1(\mathbf{x}_{k-1}) \\ f_2(\mathbf{x}_{k-1}) \\ f_3(\mathbf{x}_{k-1}) \\ f_4(\mathbf{x}_{k-1}) \end{bmatrix}, \tag{A9}$$

with

$$\mathbf{a}_1 = [1 \quad 0 \quad \eta_3 \quad -\eta_4]', \tag{A10}$$

$$\mathbf{a}_2 = [0 \quad 1 \quad \eta_4 \quad \eta_3]', \tag{A11}$$

$$\mathbf{a}_3 = [0 \quad 0 \quad \eta_2 \quad -\eta_1]', \tag{A12}$$

$$\mathbf{a}_4 = [0 \quad 0 \quad \eta_1 \quad \eta_2]'. \tag{A13}$$

By dropping the subscript  $k - 1$  from  $\mathbf{x}_{k-1}$ , we obtain

$$f_i(\mathbf{x}) = \mathbf{a}'_i \mathbf{x}, \quad i = 1, 2, \dots, 4. \tag{A14}$$

Let

$$\mathbf{x} = [x \quad y \quad \dot{x} \quad \dot{y}]'. \tag{A15}$$

By using (A9)–(A15), we obtain

$$f_1(\mathbf{x}) = x + \eta_3 \dot{x} - \eta_4 \dot{y}, \tag{A16}$$

$$f_2(\mathbf{x}) = y + \eta_4 \dot{x} + \eta_3 \dot{y}, \tag{A17}$$

$$f_3(\mathbf{x}) = \eta_2 \dot{x} - \eta_1 \dot{y}, \tag{A18}$$

$$f_4(\mathbf{x}) = \eta_1 \dot{x} + \eta_2 \dot{y}, \tag{A19}$$

By differentiating  $f_1(\mathbf{x}), f_2(\mathbf{x}), f_3(\mathbf{x})$  and  $f_4(\mathbf{x})$  with respect to  $\mathbf{x}$ , we obtain

$$\frac{\partial f_1(\mathbf{x})}{\partial \mathbf{x}} = \begin{bmatrix} 1 & 0 & (\eta_3 + \dot{x} \frac{\partial \eta_3}{\partial \dot{x}} - \dot{y} \frac{\partial \eta_4}{\partial \dot{x}}) & (\dot{x} \frac{\partial \eta_3}{\partial \dot{y}} - \eta_4 - \dot{y} \frac{\partial \eta_4}{\partial \dot{y}}) \end{bmatrix}, \tag{A20}$$

$$\frac{\partial f_2(\mathbf{x})}{\partial \mathbf{x}} = \begin{bmatrix} 0 & 1 & (\eta_4 + \dot{x} \frac{\partial \eta_4}{\partial \dot{x}} + \dot{y} \frac{\partial \eta_3}{\partial \dot{x}}) & (\dot{x} \frac{\partial \eta_4}{\partial \dot{y}} + \eta_3 + \dot{y} \frac{\partial \eta_3}{\partial \dot{y}}) \end{bmatrix}, \tag{A21}$$

$$\frac{\partial f_3(\mathbf{x})}{\partial \mathbf{x}} = \begin{bmatrix} 0 & 0 & (\eta_2 + \dot{x} \frac{\partial \eta_2}{\partial \dot{x}} - \dot{y} \frac{\partial \eta_1}{\partial \dot{x}}) & (\dot{x} \frac{\partial \eta_2}{\partial \dot{y}} - \eta_1 - \dot{y} \frac{\partial \eta_1}{\partial \dot{y}}) \end{bmatrix}, \tag{A22}$$

$$\frac{\partial f_4(\mathbf{x})}{\partial \mathbf{x}} = \begin{bmatrix} 0 & 0 & (\eta_1 + \dot{x} \frac{\partial \eta_1}{\partial \dot{x}} + \dot{y} \frac{\partial \eta_2}{\partial \dot{x}}) & (\dot{x} \frac{\partial \eta_1}{\partial \dot{y}} + \eta_2 + \dot{y} \frac{\partial \eta_2}{\partial \dot{y}}) \end{bmatrix}. \tag{A23}$$

The derivatives of  $\eta_i$  with respect to  $\mathbf{x}$  can be expressed as

$$\frac{\partial \eta_i}{\partial \mathbf{x}} = \frac{\partial \eta_i}{\partial \omega} \frac{\partial \omega}{\partial \mathbf{x}}, \quad i = 1, 2, 3, 4. \tag{A24}$$

Since  $\omega$  is a function of  $\dot{x}$  and  $\dot{y}$  only,

$$\frac{\partial \omega}{\partial x} = \frac{\partial \omega}{\partial y} = 0. \tag{A25}$$

From the expression of  $\omega$  in (A3), we obtain

$$\frac{\partial \omega}{\partial \dot{x}} = \frac{-ka\dot{x}}{(\dot{x}^2 + \dot{y}^2)^{3/2}} \tag{A26}$$

$$\frac{\partial \omega}{\partial \dot{y}} = \frac{-ka\dot{y}}{(\dot{x}^2 + \dot{y}^2)^{3/2}}. \tag{A27}$$

Hence

$$\frac{\partial \omega}{\partial \mathbf{x}} = \begin{bmatrix} 0 & 0 & \frac{\partial \omega}{\partial \dot{x}} & \frac{\partial \omega}{\partial \dot{y}} \end{bmatrix}. \tag{A28}$$

Next, we describe the computation of  $\frac{\partial \eta_i}{\partial \omega}, i = 1, 2, \dots, 4$ .

From (A4)–(A7), we obtain

$$\frac{\partial \eta_1}{\partial \omega} = T \cos \omega T. \tag{A29}$$

$$\frac{\partial \eta_2}{\partial \omega} = -T \sin \omega T. \tag{A30}$$

$$\frac{\partial \eta_3}{\partial \omega} = -\frac{\eta_1}{\omega^2} + \frac{1}{\omega} \frac{\partial \eta_1}{\partial \omega} = \frac{1}{\omega^2} [\omega \frac{\partial \eta_1}{\partial \omega} - \eta_1]. \tag{A31}$$

$$\frac{\partial \eta_4}{\partial \omega} = -\frac{1}{\omega^2} [1 - \eta_2 + \omega \frac{\partial \eta_2}{\partial \omega}]. \tag{A32}$$

This completes the derivative of the nonlinear time evolution function  $f(\mathbf{x})$  with respect to  $\mathbf{x}$ . Hence

$$\bar{\mathbf{F}}(\mathbf{x}) = \begin{bmatrix} \frac{\partial f_1(\mathbf{x})}{\partial \mathbf{x}} & \frac{\partial f_2(\mathbf{x})}{\partial \mathbf{x}} & \frac{\partial f_3(\mathbf{x})}{\partial \mathbf{x}} & \frac{\partial f_4(\mathbf{x})}{\partial \mathbf{x}} \end{bmatrix}. \quad (\text{A33})$$

## Appendix B

Appendix B presents the expressions for the derivatives of the nonlinear measurement function with respect to the state vector (Jacobian matrix used in EKF or PCRLB computation). The measurement model is explained in Section 3. Define

$$\mathbf{x} := \begin{bmatrix} \mathbf{p} \\ \mathbf{v} \end{bmatrix}. \quad (\text{A34})$$

The derivatives of the range, azimuth, and radial velocity with respect to the state vector are given by

$$\frac{\partial \xi}{\partial \mathbf{x}} = \begin{bmatrix} \frac{\partial \xi}{\partial \mathbf{p}} & \frac{\partial \xi}{\partial \mathbf{v}} \end{bmatrix}, \text{ for } \xi = r, \beta, v_r. \quad (\text{A35})$$

We can show that

$$\frac{\partial r}{\partial \mathbf{x}} = \begin{bmatrix} \mathbf{u}' & \mathbf{0}_{1 \times 2} \end{bmatrix}, \quad (\text{A36})$$

$$\frac{\partial \beta}{\partial \mathbf{x}} = \begin{bmatrix} \frac{u_y}{r} & -\frac{u_x}{r} & \mathbf{0}_{1 \times 2} \end{bmatrix}, \quad (\text{A37})$$

$$\frac{\partial v_r}{\partial \mathbf{x}} = \begin{bmatrix} \frac{\mathbf{v}'}{r} [\mathbf{I}_2 - \mathbf{u}\mathbf{u}'] & \mathbf{u}' \end{bmatrix}, \quad (\text{A38})$$

where  $\mathbf{u}$  is a unit vector along the RLOS or range vector.

Hence

$$\bar{\mathbf{H}}(\mathbf{x}) = \begin{bmatrix} \frac{\partial r}{\partial \mathbf{x}} & \frac{\partial \beta}{\partial \mathbf{x}} & \frac{\partial v_r}{\partial \mathbf{x}} \end{bmatrix}. \quad (\text{A39})$$

## References

- Li, X.R.; Jilkov, V. Survey of maneuvering target tracking, Part I: Dynamic Models. *IEEE Trans. Aerosp. Electron. Syst.* **2003**, *39*, 1333–1364.
- Zhu, W.; Wang, W.; Yuan, G. An Improved Interacting Multiple Model Filtering Algorithm Based on the Cubature Kalman Filter for Maneuvering Target Tracking. *Sensors* **2016**, *16*, 805. [[CrossRef](#)] [[PubMed](#)]
- Liu, H.; Zhou, Z.; Yang, H. Tracking maneuver target using interacting multiple model-square root cubature Kalman filter based on range rate measurement. *Int. J. Distrib. Sens. Netw.* **2017**, *13*, 1–11. [[CrossRef](#)]
- Radhakrishnan, R.; Singh, A.K.; Bhaumik, S.; Tomar, N.K. IMM-Cubature quadrature Kalman filter for manoeuvring target tracking. In Proceedings of the 2015 IEEE International Conference on Signal Processing, Informatics, Communication and Energy Systems (SPICES), Kozhikode, India, 19–21 February 2015; pp. 1–5.
- Arulampalam, S.A.; Ristic, B.; Gordon, N.; Mansell, T. Bearings-only tracking of maneuvering targets using particle filters. *EURASIP J. Appl. Signal Process.* **2004**, *15*, 2351–2365.
- Kalman, R.E. A new approach to linear filtering and prediction problems. *Trans. ASME J. Basic Eng.* **1960**, *82*, 35–45. [[CrossRef](#)]
- Anderson, B.D.O.; Moore, J.B. *Optimal Filtering*; Prentice-Hall: Englewood Cliffs, NJ, USA, 1979.
- Bar-Shalom, Y.; Li, X.R.; Kirubarajan, T. *Estimation with Applications to Tracking and Navigation*; Wiley: New York, NY, USA, 2001.
- Mendel, J.M. *Lessons in Estimation Theory for Signal Processing, Communications, and Control*; Prentice Hall: Englewood Cliffs, NJ, USA, 1995.
- Grewal, M.S.; Andrews, A.P. *Kalman Filtering: Theory and Practice with MATLAB*; John Wiley & Sons: Hoboken, NJ, USA, 2014.
- Simon, D. *Optimal State Estimation: Kalman, H Infinity, and Nonlinear Approaches*; John Wiley & Sons: Hoboken, NJ, USA, 2006.
- Schmidt, S.F. The Kalman filter: Its recognition and development for aerospace applications. *J. Guid. Control Dyn.* **1981**, *4*, 4–7. [[CrossRef](#)]
- Magee, L.A.; Schmidt, S.F. *Discovery of the Kalman Filter as a Practical Tool for Aerospace and Industry*; Technical Report Technical Memorandum 86847; NASA, Ames Research Center: Moffett Field, CA, USA, 1985.
- Julier, S.; Uhlmann, J.; Durrant-Whyte, H. A new method for the nonlinear transformation of means and covariances in filters and estimators. *IEEE Trans. Autom. Control* **2000**, *45*, 477–482. [[CrossRef](#)]
- Julier, S.J.; Uhlmann, J.K. Unscented filtering and nonlinear estimation. *Proc. IEEE* **2004**, *92*, 401–422. [[CrossRef](#)]
- Ito, K.; Xiong, K.Q. Gaussian filters for nonlinear filtering problems. *IEEE Trans. Autom. Control* **2000**, *45*, 910–927. [[CrossRef](#)]
- Norgaard, M.; Poulsen, N.K.; Ravn, O. New developments in state estimation for nonlinear systems. *Automatica* **2000**, *36*, 1627–1638. [[CrossRef](#)]

18. Arasaratnam, I.; Haykin, S. Cubature Kalman filters. *IEEE Trans. Autom. Control* **2009**, *54*, 1254–1269. [[CrossRef](#)]
19. Arulampalam, M.; Maskell, S.; Gordon, N.; Clapp, T. A tutorial on particle filters for online nonlinear/non-Gaussian Bayesian tracking. *IEEE Trans. Signal Process.* **2002**, *50*, 174–188. [[CrossRef](#)]
20. Ristic, B.; Arulampalam, S.; Gordon, N. *Beyond the Kalman Filter*; Artech House: Norwood, MA, USA, 2004.
21. Doucet, A.; Johansen, A.M. A Tutorial on Particle Filtering and Smoothing: Fifteen Years Later. *Handb. Nonlinear Filter.* **2009**, *12*, 656–704.
22. Gustafsson, F. Particle Filter Theory and Practice with Positioning Applications. *IEEE Aerosp. Electron. Syst. Mag.* **2010**, *25*, 53–82. [[CrossRef](#)]
23. Wu, Y.; Hu, D.; Wu, M.; Hu, X. A numerical-integration perspective on Gaussian filters. *IEEE Trans. Signal Process.* **2006**, *54*, 2910–2921. [[CrossRef](#)]
24. Mallick, M.; Arulampalam, S. Comparison of nonlinear filtering algorithms in ground moving target indicator (GMTI) target tracking. *Proc. SPIE* **2003**, *5204*, 630–647.
25. Mazor, E.; Averbuch, A.; Bar-Shalom, Y.; Dayan, J. Interacting multiple model methods in target tracking: A survey. *IEEE Trans. Aerosp. Electron. Syst.* **1998**, *34*, 103–123. [[CrossRef](#)]
26. Blom, H.A.P. An efficient filter for abruptly changing systems. In Proceedings of the 23rd IEEE Conference on Decision and Control, Las Vegas, NV, USA, 12–14 December 1984; pp. 656–658.
27. Blom, H.A.P.; Bar-Shalom, Y. The Interacting Multiple Model algorithm for systems with Markovian switching coefficients. *IEEE Trans. Autom. Control* **1988**, *33*, 780–783. [[CrossRef](#)]
28. Blom, H.A.P.; Hogendoorn, R.A.; van Doorn, B.A. Design of a Multisensor Tracking System for Advanced Air Traffic Control. In *Multitarget Multisensor Tracking: Applications and Advances*; Bar-Shalom, Y., Ed.; Artech House: Norwood, MA, USA, 1992; pp. 31–63.
29. Li, X.R.; Bar-Shalom, Y. Design of an interacting multiple model algorithm for air traffic control tracking. *IEEE Trans. Control Syst. Technol.* **1993**, *1*, 186–194. [[CrossRef](#)]
30. Kastella, K.; Biscuso, M. Tracking algorithms for air traffic control applications. *Air Traffic Control. Q.* **1996**, *3*, 19–43. [[CrossRef](#)]
31. Jilkov, V.P.; Angelova, D.S.; Semerdjiev, T.Z.A. Design and comparison of mode-set adaptive IMM algorithms for maneuvering target tracking. *IEEE Trans. Aerosp. Electron. Syst.* **1999**, *35*, 343–350. [[CrossRef](#)]
32. Blackman, S.S.; Dempster, R.J.; Blyth, B.; Durand, C. Integration of passive ranging with multiple hypothesis tracking (MHT) for application with angle-only measurements. *Proc. SPIE* **2010**, *7698*, 769815-1–769815-11.
33. Yeddapanudi, M.; Bar-Shalom, Y.; Pattipati, K.R. IMM estimation for multitarget-multisensor air traffic surveillance. *Proc. IEEE* **1997**, *85*, 80–94. [[CrossRef](#)]
34. Wang, H.; Kirubarajan, T.; Bar-Shalom, Y. Precision large scale air traffic surveillance using IMM/assignment estimators. *IEEE Trans. Aerosp. Electron. Syst.* **1999**, *35*, 255–266. [[CrossRef](#)]
35. Johnston, L.A.; Krishnamurthy, V. An improvement to the interacting multiple model (IMM) algorithm. *IEEE Trans. Signal Process.* **2001**, *49*, 2909–2923. [[CrossRef](#)]
36. Bar-Shalom, Y.; Challa, S.; Blom, H.A.P. IMM estimator versus optimal estimator for hybrid systems. *IEEE Trans. Aerosp. Electron. Syst.* **2005**, *41*, 986–991. [[CrossRef](#)]
37. Li, X.R.; Bar-Shalom, Y. Performance Prediction of the Interacting Multiple Model Algorithm. *IEEE Trans. Aerosp. Electron. Syst.* **1993**, *29*, 755–771. [[CrossRef](#)]
38. Bar-Shalom, Y.; Willett, P.; Tian, X. *Tracking and Data Fusion: A Handbook of Algorithms*; YBS Publishing: Storrs, CT, USA, 2011.
39. Kurien, T. Issues in the design of practical multitarget tracking algorithms. In *Multitarget-Multisensor Tracking: Advanced Applications*; Bar-Shalom, Y., Ed.; Artech House: Norwood, MA, USA, 1990; pp. 43–83.
40. Blackman, S.; Popoli, R. *Design and Analysis of Modern Tracking Systems*; Artech House: Norwood, MA, USA, 1999.
41. Vo, B.N.; Mallick, M.; Bar-shalom, Y.; Osborne, R.; Vo, B.T. Multitarget tracking. In *Wiley Encyclopedia of Electrical and Electronics Engineering*; Wiley: New York, NY, USA, 2015; pp. 1–35.
42. Mahler, R. *Advances in Statistical Multisource-Multitarget Information Fusion*; Artech House: Norwood, MA, USA, 2014.
43. Puranik, S.; Tugnait, J.K. Tracking of Multiple Maneuvering Targets using Multiscan JPDA and IMM Filtering. *IEEE Trans. Aerosp. Electron. Syst.* **2007**, *43*, 23–35. [[CrossRef](#)]
44. Coraluppi, S. Fundamentals and Advances in Multiple-Hypothesis Tracking. Technical Report, NATO STO IST-134 Lecture Series, 2015. Lecture Series on Advanced Algorithms for Effectively Fusing Hard and Soft Information. Available online: <https://www.semanticscholar.org/paper/Fundamentals-and-Advances-in-Multiple-Hypothesis-Coraluppi/fc01033561818ff3378a0d9245794792461af585> (accessed on 2 September 2024).
45. Beard, M.; Vo, B.T.; Vo, B.N. A Solution for Large-Scale Multi-Object Tracking. *IEEE Trans. Signal Process.* **2020**, *68*, 2754–2769. [[CrossRef](#)]
46. Blackman, S.S.; Dempster, R.J.; Busch, M.T.; Popoli, R.F. IMM/MHT solution to radar benchmark tracking problem. *IEEE Trans. Aerosp. Electron. Syst.* **1999**, *35*, 730–738. [[CrossRef](#)]
47. Punithakumar, K.; Kirubarajan, T.; Sinha, A. Multiple-model probability hypothesis density filter for tracking maneuvering targets. *IEEE Trans. Aerosp. Electron. Syst.* **2008**, *44*, 87–98. [[CrossRef](#)]
48. Mallick, M.; Coraluppi, S.; Carthel, C. Multitarget tracking using multiple hypotheses tracking. In *Integrated Tracking, Classification, and Sensor Management: Theory and Applications*; Wiley/IEEE: Hoboken, NJ, USA, 2012; Chapter 5, pp. 165–201.

49. Tapley, B.D.; Schutz, B.E.; Born, G.H. *Statistical Orbit Determination*; Elsevier Academic Press: Burlington, MA, USA, 2004.
50. Jazwinski, A.H. *Stochastic Processes and Filtering Theory*; Academic Press: San Diego, CA, USA, 1970.
51. Radhika, M.N.; Parthasarathy, S.S.; Mallick, M. Numerical Simulation of a Highly Maneuvering Target in 2D Using the Bayesian Framework. *Int. J. Sci. Technol. Res.* **2020**, *9*, 3262–3269.
52. Mallick, M.; Chang, K.C.; Arulampalam, S.; Yan, Y. Heterogeneous Track-to-Track Fusion in 3D UsingIRST Sensor and Air MTI Radar. *IEEE Trans. Aerosp. Electron. Syst.* **2019**, *55*, 3062–3079. [[CrossRef](#)]
53. Mallick, M.; La Scala, B.F. IMM Estimator for Ground Target Tracking with Variable Measurement Sampling Intervals. In Proceedings of the 2006 9th International Conference on Information Fusion, Florence, Italy, 10–13 July 2006; pp. 1–8.
54. Kim, Y.S.; Hong, K.S. An IMM algorithm for tracking maneuvering vehicles in an adaptive cruise control environment. *Int. J. Control Autom. Syst.* **2004**, *2*, 310–318.
55. Farina, A.; Immediata, S.; Timmoneri, L. Impact of ballistic target model uncertainty on IMM-UKF and IMM-EKF tracking accuracies. In Proceedings of the 14th European Signal Processing Conference (EUSIPCO 2006), Florence, Italy, 4–8 September 2006.
56. Bugallo, M.F.; Xu, S.; Djuric, P.M. Performance comparison of IMM-EKF and particle filtering methods for maneuvering targets. *Digit. Signal Process.* **2007**, *17*, 774–786. [[CrossRef](#)]
57. Djouadi, M.S.; Sebbagh, A.; Berkani, D. IMM-UKF algorithm and IMM-EKF algorithm for tracking highly maneuverable target: A comparison. In Proceedings of the WSEAS International Conference on Automatic Control Modeling and Simulation, Prague, Czech Republic, 13–15 March 2005; pp. 283–286.
58. Wan, M.; Li, P.; Li, T. Tracking Maneuvering Target with Angle-only Measurements Using IMM Algorithm Based on CKF. In Proceedings of the 2010 International Conference on Communications and Mobile Computing, Shenzhen, China, 12–14 April 2010.
59. Van Trees, H.L.; Bell, K.L.; Tian, Z. *Detection, Estimation, and Modulation Theory, Part I: Detection, Estimation, and Filtering Theory*, 2nd ed.; John Wiley & Sons: Hoboken, NJ, USA, 2013.
60. Tichavsky, P.; Muravchik, C.H.; Nehorai, A. Posterior Cramér-Rao bounds for discrete-time nonlinear filtering. *IEEE Trans. Signal Process.* **1998**, *46*, 1386–1396. [[CrossRef](#)]
61. Hernandez, M. Performance bounds for target tracking: Computationally efficient formulations and associated applications. In *Integrated Tracking, Classification, and Sensor Management: Theory and Applications*; Wiley/IEEE: Hoboken, NJ, USA, 2012; Chapter 7, pp. 255–310.
62. Li, X.R.; Zhao, Z.; Jilkov, V.P. Estimator’s credibility and its measures. In Proceedings of the IFAC 15th World Congress, Barcelona, Spain, 21–26 July 2002.
63. Mallick, M.; Arulampalam, S.; Yan, J.; Ru, S. Three Dimensional Tracking of an Aircraft Using 2D Radars. *IEEE Trans. Aerosp. Electron. Syst.* **2018**, *54*, 585–600. [[CrossRef](#)]
64. Mallick, M.; Nagaraju, R.M.; Duan, Z. IMM-CKF for a Highly Maneuvering Target Using Converted Measurements. In Proceedings of the 2021 International Conference on Control, Automation and Information Sciences (ICCAIS), Xi’an, China, 14–17 October 2021; pp. 15–20.
65. Radhika, M.N.; Mallick, M.; Tian, X.; Liu, J. Performance Evaluation of IMM-based Nonlinear Filters for a Highly Maneuvering Aircraft. In Proceedings of the 2021 International Conference on Control, Automation and Information Sciences (ICCAIS), Xi’an, China, 14–17 October 2021; pp. 549–555.
66. Talebi, S.P.; Godsill, S.J.; Mandic, D.P. Filtering Structures for  $\alpha$ -Stable Systems. *IEEE Control Syst. Lett.* **2023**, *7*, 553–558. [[CrossRef](#)]

**Disclaimer/Publisher’s Note:** The statements, opinions and data contained in all publications are solely those of the individual author(s) and contributor(s) and not of MDPI and/or the editor(s). MDPI and/or the editor(s) disclaim responsibility for any injury to people or property resulting from any ideas, methods, instructions or products referred to in the content.